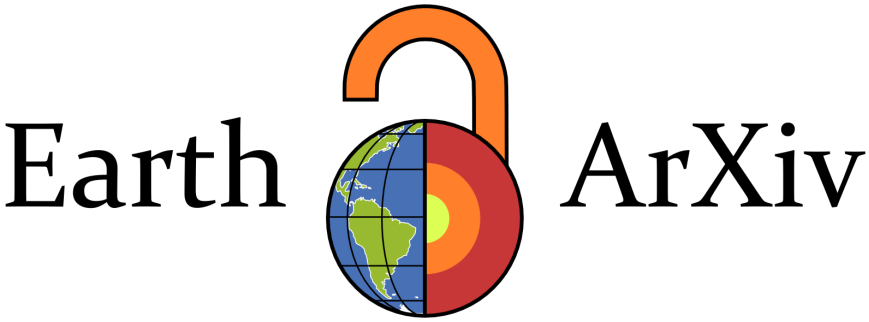

Fine-scale Segmentation and Spatiotemporal Variability of the 2010 Mw 8.8 Maule Aftershock Sequence Revealed by a Deep-Learning-Based Earthquake Catalog

Rodrigo Flores-Allende[1], Léonard Seydoux[1], Éric Beaucé[2,3], Luis Fabian Bonilla[3,1], Philippe Gueguen[4] and Claudio Satriano[1]

[1]Université Paris Cité, Institut de physique du globe de Paris, UMR 7154, Paris, France
[2]Lamont-Doherty Earth Observatory, Columbia University, New York, NY, USA
[3]Université Gustave Eiffel, Champs-sur-Marne, Marne-la-Vallée, France
[4]ISTerre, Université Grenoble Alpes/CNRS/Univ. Savoie Mont-Blanc/IRD/Université Gustave Eiffel, 38000 Grenoble, France

Corresponding author: floresallende@ipgp.fr

Peer-review status:

This manuscript has been submitted to Journal of Geophysical Research: Solid Earth and is currently under review. It has not yet been formally accepted for publication. Subsequent versions of this manuscript may differ from this version.

Fine-scale Segmentation and Spatiotemporal Variability of the 2010 M_w 8.8 Maule Aftershock Sequence Revealed by a Deep-Learning-Based Earthquake Catalog

Rodrigo Flores-Allende[1], Léonard Seydoux[1], Éric Beaucé[2], Luis Fabian Bonilla[3,1], Philippe Gueguen[4] and Claudio Satriano[1]

[1]Université Paris Cité, Institut de Physique du Globe de Paris, UMR 7154, Paris, France
[2]Lamont-Doherty Earth Observatory, Columbia University, New York, NY, USA
[3]Université Gustave Eiffel, Champs-sur-Marne, Marne-la-Vallée, France
[4]ISTerre, Université Grenoble Alpes/CNRS/Univ. Savoie Mont-Blanc/IRD/Université Gustave Eiffel, 38000 Grenoble, France

Key Points:

- We build a dense catalog of 537,390 aftershocks of the 2010 M_w 8.8 Maule earthquake, achieving a completeness magnitude of about M_w 1.8.
- Automated detection and relocation yield consistent magnitudes and improved locations across variable network coverage.
- Spatial b-values vary along strike, consistent with a weaker, fluid-rich northern interface and a stronger southern megathrust.

Corresponding author: Rodrigo Flores-Allende, `floresallende@ipgp.fr`

Abstract

We re-examine the aftershock sequence of the M_w 8.8 Maule earthquake in south-central Chile to understand how seismicity, magnitude-frequency distribution, and fault structure vary along the rupture zone. Using the International Maule Aftershock Deployment (IMAD) dataset, we analyze ten months of continuous data from 156 temporary stations and build a high-resolution aftershock catalog for the Maule rupture zone. We apply the BeamPower and Matched Filtering (BPMF) workflow, which integrates a deep-learning phase picker with backprojection-based association, relative relocation, and template matching. We initially detect and relocate 130,578 earthquakes, then use a subset of high-quality events as templates to identify smaller earthquakes missed by the initial detection. The final catalog contains about 537,390 earthquakes, nearly 13 times more than previous studies, with a completeness magnitude of $\sim M_w$ 1.8 and magnitudes ranging from M_w 0.2 to M_w 6.2. A regional local magnitude (M_L) calibration ensures homogeneous magnitude scales across the network. The dense catalog resolves detailed seismotectonic features along the rupture. In the Pichilemu region, aftershocks delineate a shallow normal fault system with L-shaped geometry, whereas the Concepción area exhibits aseismic patches. Using classical maximum likelihood and *b*-more-incomplete methods, we find that temporal *b*-values range between 1.2 and 1.6 early in the sequence and converge toward about 1.0. Meanwhile, spatial *b*-values are strongly segmented along strike, with higher values in the north and lower values in the south. These contrasts are consistent with along-strike variations in effective stress and pore fluid pressure on the plate interface, in line with previous studies.

Plain Language Summary

After a large earthquake, the Earth continues to adjust through thousands of smaller events called aftershocks. Studying when and where these aftershocks occur helps scientists understand how the fault releases stress and improves future hazard assessments. We revisit the aftershocks of the 2010 magnitude 8.8 Maule earthquake in south-central Chile using nearly a year of data from 156 temporary seismic stations. By applying modern computer-based methods, including machine learning and template matching techniques, we detect and locate many small earthquakes that were not identified before. The new earthquake catalog includes more than half a million events, about 13 times more than in previous studies, and shows that aftershocks are not distributed evenly along the fault. Near Pichilemu, they outline a shallow fault system, while deeper activity occurs within the oceanic plate that is sinking beneath South America. We also examine how the proportion of small to large earthquakes changes over time and along the fault, which provides clues about differences in stress, fluid presence, and rock strength. This study demonstrates how advanced analysis tools applied to existing data can reveal new details about how great earthquakes rupture and how subduction zones evolve over time.

1 Introduction

On February 27, 2010, a M_w 8.8 earthquake struck the Maule region in south-central Chile, causing significant loss of life and widespread damage (Salazar & McNutt, 2011). The rupture extended 500 km along the convergence margin between the Pacific and Nazca plates, between latitudes 33°S and 38.5°S (Figure 1a). This event ranks among the largest instrumentally recorded earthquakes worldwide, and is the strongest well-recorded in Chile (e.g., Delouis et al., 2010; Madariaga et al., 2010; Moreno et al., 2010; Vigny et al., 2011; S. Ruiz et al., 2012; Hicks et al., 2014; S. Ruiz & Madariaga, 2018). Its rupture coincides with the mature seismic gap left by the M_w 8.3 earthquake of 1835 (see, e.g., Campos et al., 2002), and overlaps segments of previous major earthquakes, including the M_w 7.7 Talca (1928), M_w 8.1 Concepción (1960, e.g., Ojeda et al., 2020), and M_w 7.8 Arauco (1975) earthquakes. It also partially overlaps the M_w 9.5 Valdivia earthquake area of 1960, the largest earthquake ever recorded in history (e.g., Madariaga et al., 2010; S. Ruiz et al., 2012).

Large megathrust earthquakes, such as those related to subduction zones, are typically followed by an increase in seismic activity known as aftershocks. Earthquakes are considered aftershocks when their magnitude is at least one unit smaller than the mainshock (Båth, 1965), and can persist for weeks to years (Bilek & Lay, 2018). They result from stress perturbations induced by the main rupture (Felzer et al., 2004), and their distribution across the rupture zone often correlates with regions of high postseismic strain and substantial static stress changes (Lange et al., 2012; Rietbrock et al., 2012). Among the many aftershocks of the Maule earthquake, shortly after the mainshock, two large aftershocks of M_w 6.9 and M_w 6.7 struck the area of Pichilemu on March 11, 2010, at the northern edge of the rupture zone (Farías et al., 2011; Lange et al., 2012; Rietbrock et al., 2012; Ryder et al., 2012; J. A. Ruiz et al., 2014; Jara-Muñoz et al., 2022). These aftershocks suggest a potential migration of seismicity or the reactivation of analogous fault systems in the region.

Over the past decade, the International Maule Aftershock Deployment (IMAD) dataset has been a key resource for studying the Maule aftershock sequence. Deployed within a few weeks after the mainshock (Guéguen et al., 2011), this mobile seismic network covered the entire rupture area (Figure 1a) and enabled the construction of some early earthquake catalogs. For instance, Lange et al. (2012) and Rietbrock et al. (2012) applied classical Short-Term Average to Long-Term Average (STA/LTA) automatic pickers, detecting over 20,000 events in six months and more than 30,000 events in just two months, respectively. These initial efforts provided a broad overview of the rupture segmentation, aftershock distribution, and fault reactivation. Using the catalog from Rietbrock et al. (2012); Agurto et al. (2012), they refined the locations of the largest aftershocks and performed regional moment tensor (RMT) inversions to characterize spatio-temporal variations in seismic moment release. One of the main observations was the apparent lack of large aftershocks in regions of highest coseismic slip (Agurto et al., 2012; Rietbrock et al., 2012). Although this pattern appears to depend on the selected slip model, both studies agreed that only low-magnitude seismicity was present in these high-slip patches. This emphasizes the need for accurate detection and location of small events to delineate and characterize the interaction between seismic and aseismic patches. As a result, the contribution of these regions to the total postseismic deformation budget remains unclear, and deeper intraslab contributions may also be underestimated. Moreover, Neighbors et al. (2015) estimated the high-frequency attenuation parameter κ, finding significant spatial variability likely reflecting the combined effects of source, path, and site conditions, though poorly correlated with surface geology. In parallel, Tassara et al. (2016) analyzed b-value patterns in relation to afterslip and identified contrasting mechanical domains along strike, which they related to variations in fluid content and fault rheology. While both studies provided valuable constraints, their resolution was limited by the number of events used, as they considered only a few subsets of moderate-to-large magnitude aftershocks. In this study, we build on these previous constraints using a much denser, magnitude-calibrated aftershock catalog and a b-value estimator that is less sensitive to completeness, which allows us to resolve the along-strike segmentation of the Maule rupture and to reassess the role of fluids and effective normal stress in controlling aftershock behavior.

A clear understanding of aftershock patterns, afterslip distribution, and triggering mechanisms is key to improving our knowledge of earthquake mechanics (Peng & Zhao, 2009; Yao et al., 2017; Minetto et al., 2022; Farge & Brodsky, 2025). Although often neglected in stress-transfer models, small-magnitude earthquakes can collectively have a significant impact due to their high occurrence and spatial clustering. Marsan (2005) demonstrated that stress perturbations from small earthquakes can be as influential as those from larger ones, highlighting the importance of including microseismicity in further analysis. For instance, S. Ruiz et al. (2017) used repeaters to reveal aseismic processes before and after the 2017 M_w 6.9 Valparaiso earthquake, suggesting that small-scale seismicity may have triggered the mainshock and played an important role in the rupture dynamics. However, current studies mainly rely on large-magnitude aftershocks, as detecting smaller ones remains challenging. Seismic noise often hinders the detection of low-magnitude aftershocks, particularly when

using traditional methods based on signal amplitude such as Signal-to-Noise Ratio (SNR) or the previously mentioned STA/LTA trigger (see, e.g., Allen, 1982). Other factors, such as wave scattering and attenuation, further complicate the detection of small aftershocks, especially in regions with extensive rupture zones and sparse seismic networks as in the present study (Figure 1b).

Recent advances in deep learning have significantly improved the quality of earthquake catalogs (Ross et al., 2019; Mousavi & Beroza, 2023; Zhu & Beroza, 2019). These methods excel at identifying low-magnitude events and provide more reliable locations, unveiling the intricate details of seismic sequences and fault structures (Beaucé et al., 2019; Tan et al., 2021; Beaucé et al., 2022; Mancini et al., 2022; Minetto et al., 2022). In this study, we use these techniques to reassess an old, but distinctive dataset recorded by the IMAD network (Beck et al., 2014). We build a high resolution earthquake catalog of the Maule aftershock sequence and analyze how seismicity is distributed in space and time across the rupture zone. Our goal is to resolve how aftershock distribution, magnitude statistics, and fault structure vary along the Maule rupture zone, which remained only partially imaged in previous studies. We pursue three main objectives. First, we construct a dense and internally consistent catalog under strongly variable station coverage, combining automatic phase picking, backprojection-based association, and two relocation stages, so that small earthquakes can be used reliably to map fine-scale structures and stress heterogeneity. Second, we calibrate a regional local magnitude scale directly from Maule waveforms and reference moment magnitudes, and use it to obtain homogeneous M_L and M_w for all events. Third, we map spatial and temporal variations of the b-value and magnitude of completeness, and relate these patterns to the segmented plate interface and to the Pichilemu crustal fault system.

To achieve this, we follow the BeamPower and Matched Filtering (BPMF) strategy of Beaucé et al. (2024), combining the deep-neural-network seismic phase picking PhaseNet (Zhu & Beroza, 2019) with backprojection (Frank & Shapiro, 2014) to detect and locate earthquakes, and two relocation stages with NonLinLoc (Lomax, 2001; Lomax & Savvaidis, 2022) to build an initial catalog. We then apply a template matching to these well located events (Gibbons & Ringdal, 2006; Frank & Shapiro, 2014; Beaucé et al., 2018) to identify additional earthquakes that would otherwise be missed by conventional techniques, increasing the catalog completeness and extending the magnitude range (Minetto et al., 2022).

In the following sections, we first outline the tectonic context of south-central Chile, with a focus on the 2010 Maule earthquake and its aftershock sequence. We then describe the IMAD database and the BPMF method used for earthquake detection, association, and relocation, and we summarize the resulting catalog. Next, we present the magnitude calibration, derive homogeneous M_L and M_w, and perform a Gutenberg–Richter analysis, including a recent method for estimating the b-value that is less sensitive to time-dependent completeness. Finally, we analyze the spatiotemporal distribution of seismicity, compare the new catalog to previous ones, and discuss the implications for rupture segmentation and the Pichilemu fault system.

2 Geotectonic setting

The Maule segment of the south-central Chilean subduction zone (33 - 39 S) is a tectonically transitional region that accommodates oblique convergence between the Nazca and South American plates at approximately 66 mm/year (Haberland et al., 2009). This segment is bounded by the subducted Juan Fernández Ridge to the north and the Mocha Fracture Zone to the south, and marks a transition from a strongly coupled interface in central Chile to a more weakly coupled regime farther south (Moreno et al., 2010; Vigny et al., 2011). The segmentation is shaped by inherited lithospheric discontinuities, including the Lanalhue Fault Zone and terrane boundaries across a metamorphic Paleozoic basement intruded by Mesozoic granitoids (Hervé et al., 1987, 1988; Mpodozis & Ramos, 1990; Glodny et al., 2008; Aron et al., 2015). These crustal features influence upper-plate faulting, forearc

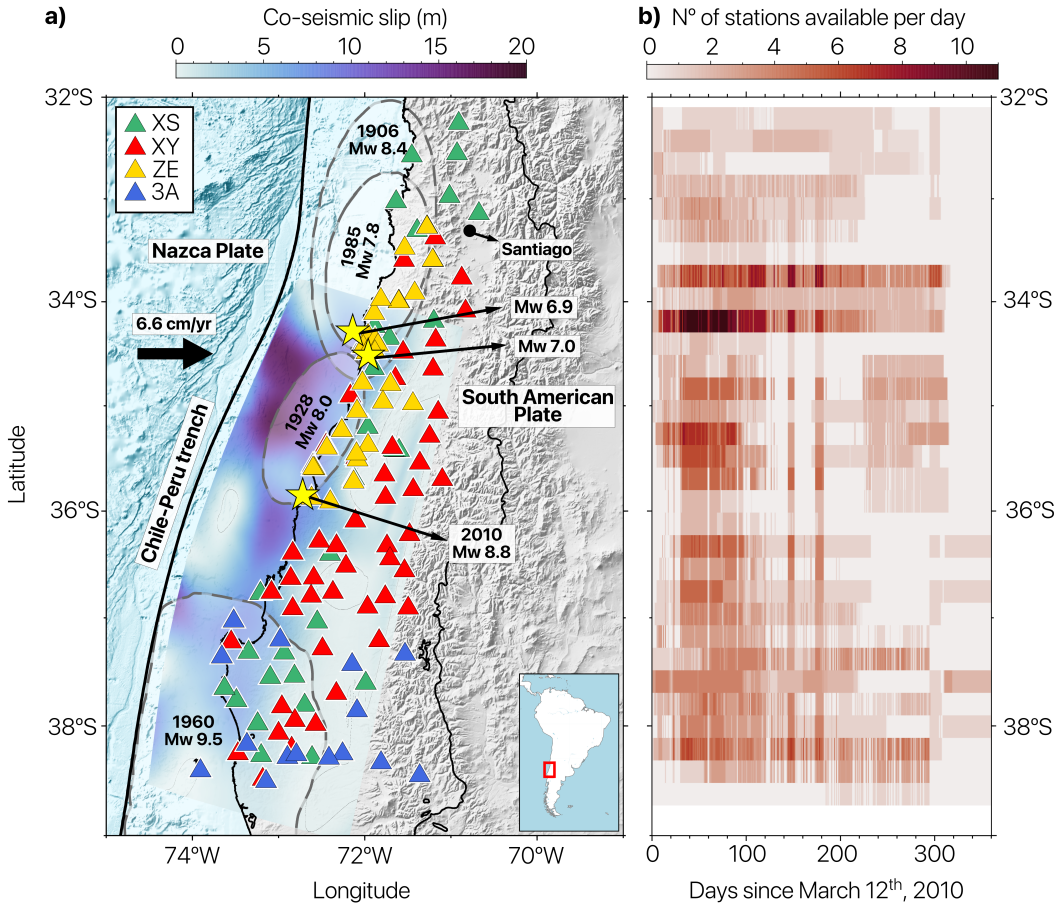

Figure 1. Study area and data coverage. **(a)** Seismic stations deployed in south-central Chile after the mainshock (triangles). Each color represents a network managed by different institutions: RESIF (XS in green, Vilotte et al., 2011), University of Florida (XY in red Steve Roecker & Ray Russo, 2010), GFZ (ZE in yellow), and University of Liverpool (3A in blue, Beck et al., 2014). The coseismic slip model presented by (Yue et al., 2014) is represented in background colors, with darker zones related to larger slip. The yellow star marks the location of the M_w 8.8 mainshock on February 27, 2010, as well as the largest aftershocks in the Pichilemu zone (34°30'S), with magnitudes M_w 6.9 and M_w 7.0, respectively. Historical rupture areas are depicted with gray ellipses. **(b)** Spatiotemporal availability of data. The color indicates the daily density of stations available every 0.2° of latitude.

uplift, and variations in mechanical coupling (Melnick et al., 2009). This geotectonically complex segment ruptured during the M_w 8.8 mainshock and is believed to have released the strain accumulated since 1835 (Campos et al., 2002; Ruegg et al., 2009). The rupture nucleated near 36.5 S and propagated bilaterally, producing two major slip patches, a northern one with a peak up to 20 m, overlapping the probable 1928 rupture zone and extending north toward the 1985 rupture border, and a southern one, with approximately 10 m of slip overlapping the northern edge of the 1960 M_w 9.5 rupture zone (Figure 1a; Delouis et al., 2010; Lorito et al., 2011; Pollitz et al., 2011; S. Ruiz et al., 2012; Yue et al., 2014). Despite its magnitude, the Maule earthquake may not have fully released all the accumulated stress (Madariaga et al., 2010; Moreno et al., 2010), underscoring the role of margin segmentation and structural inheritance in governing rupture propagation and seismic potential. Alongstrike changes in plate coupling, coseismic slip, and forearc structure suggest a segmented behavior of the Maule rupture, with contrasting conditions between the northern, central, and southern segments (Moreno et al., 2010; J. A. Ruiz et al., 2014; Tassara et al., 2016). The crustal Pichilemu fault system accommodates part of the shallow extension above the plate interface and hosts intense upper-crustal seismicity during the aftershock phase (Farías et al., 2011; Rietbrock et al., 2012). These contrasts in structure and kinematics provide a natural framework to interpret spatial variations in frequency–magnitude statistics and b-values, and to relate them to differences in coupling, stress conditions, and fluid content along the margin.

3 Data and Preprocessing

We retrieve one year of seismic data from the IMAD dataset, which corresponds to a postseismic mobile network operated by France, the United States, Germany, the United Kingdom, and collaborating partners, covering from March 2010 to March 2011 (see, e.g., Beck et al., 2014). This seismic array included nearly 156 instruments equipped with accelerometers, short-period seismometers, and broadband seismometers (Figure 1a). Stations were deployed across the entire rupture area (Figure 1a), though not all operated simultaneously or for the same durations (Figure 1b). Also, external conditions caused fluctuations in station availability over time, making the dataset less stable and uniform (Lange et al., 2012), so that at certain periods, fewer than 20 stations were operational, while at most, nearly 120 stations were simultaneously active.

To mitigate this variability, we exclude stations and traces with substantial data gaps. In regions with multiple stations within a 500 m radius, we select one station to avoid redundancy. Finally, we focus on periods with consistent availability of at least five stations, defined as the lowest threshold providing sufficient spatial and temporal coverage. This minimum threshold does not vary across the study area or over time, although the specific station combinations may change depending on the variable network configuration. The sequential steps of the workflow are illustrated in Figure 2, with further details provided in the subsequent sections.

We bandpass-filter the continuous data between 1 and 20 to discard low-frequency noise. We select this frequency range from an initial visual inspection of the data, which show energy concentrations mainly above 1 Hz. This approach is consistent with the parameters applied by Cabrera et al. (2021) in a similar tectonic context. Continuous waveforms were processed at the native sampling rates of each station, keeping them for the detection, relocation and magnitude estimation stages. In addition, we ensure the inclusion of only stations with minimal data gaps and consistent operational records. We include data segments if they meet two key criteria: (1) a minimum total duration of 75 % of the expected recording period for the event or station, ensuring sufficient temporal coverage despite potential gaps, and (2) individual contiguous chunks with a duration of at least 600 s, excluding excessively short fragments unsuitable for the analysis.

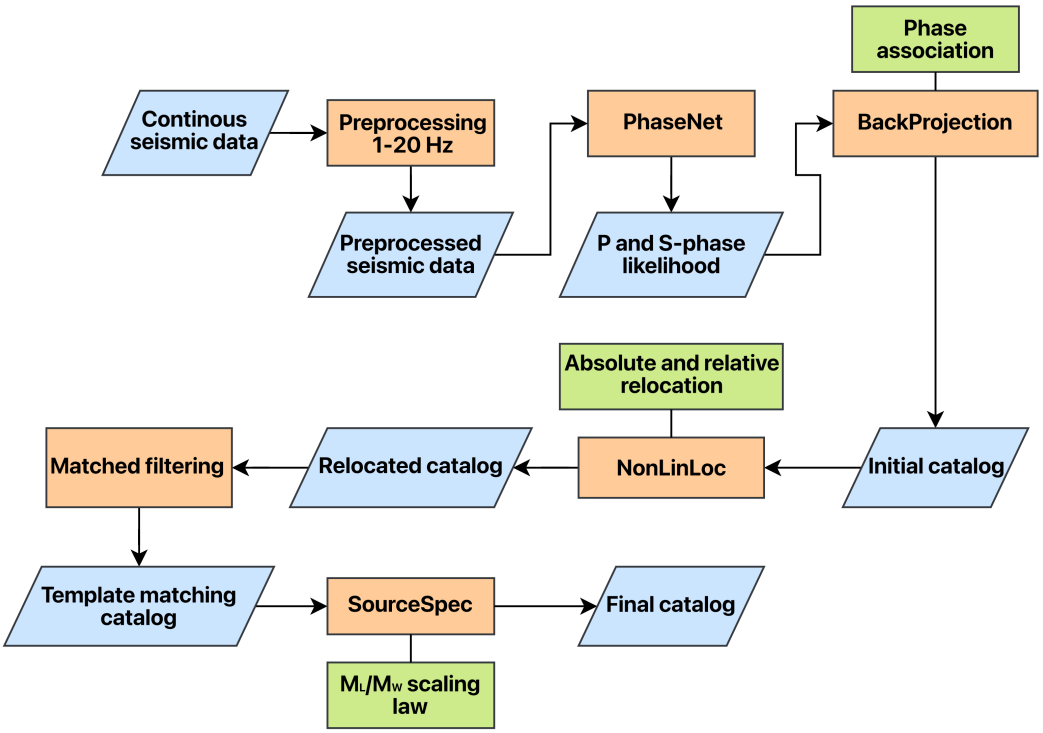

Figure 2. Earthquake catalog workflow. Blue boxes represent data (inputs or outputs), orange boxes indicate operations, and green boxes highlight some key steps. Continuous seismic data are filtered between 1 and 20 Hz and processed with PhaseNet to identify P and S-phase likelihoods. We associate the phases in space with backprojection to detect and locate the initial events, and relocate them with NonLinLoc. Additional techniques, such as template matching, contribute to increase the catalog completeness, while SourceSpec enables the magnitude estimation.

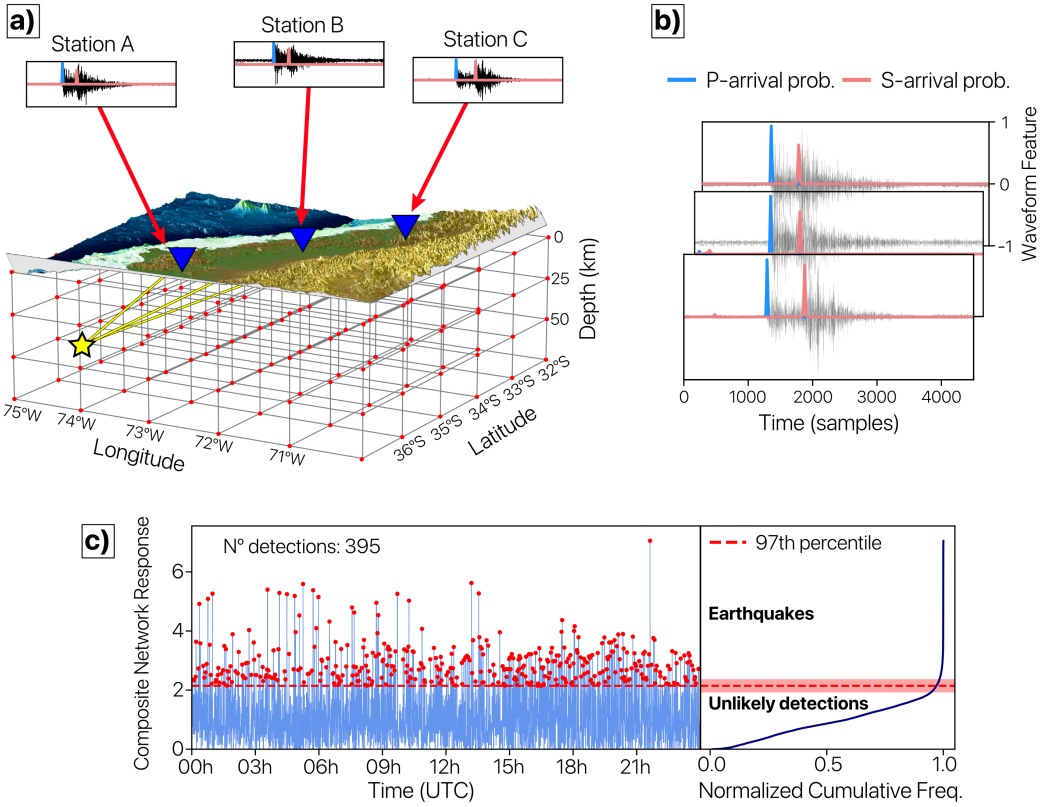

Figure 3. Earthquake detection and initial location. **(a)** Illustration of the grid with tested source points. The yellow star indicates the true earthquake location, with corresponding signals recorded at the seismic stations. **(b)** Example seismic record with the P and S likelihoods obtained using PhaseNet (Zhu & Beroza, 2019), shown in blue and orange, respectively. **(c)** Composite network response obtained by shifting and stacking the waveform features for each component and station over time (Beaucé et al., 2024). The detection threshold is indicated with a dashed red line, with red points indicating events interpreted as localized sources.

This workflow is based on the BPMF algorithm (Beaucé et al., 2024) whose outputs are post-processed with the NonLinLoc, Source-Specific Station Term (SSST) correction and waveform coherence relocation algorithm (Lomax & Savvaidis, 2022) to enhance earthquake locations, and SourceSpec to estimate the moment magnitudes (Satriano, 2021). These tools complement the original framework and were included to increase the robustness of the results.

4 Earthquake Catalog

4.1 Detection and Phase Association

To detect and locate the initial earthquakes, we build a 3D spatial grid of potential point sources (Figure 3a). The grid covers the full extent of the rupture area, with a horizontal spacing of 0.03° in both latitude and longitude and a vertical spacing of 0.5 , reaching depths of up to 100 . This parameterization is consistent with the effective resolution of the 3D velocity model used in this study for south-central Chile (Figure S1 in the Support-

ing Information; Potin et al., 2025) and provides a practical compromise between spatial resolution and computational cost.

We compute the P- and S-wave travel times (moveouts) τ_{sk}^{ϕ} from each grid point k to station s for the seismic phase $\phi \in \{P, S\}$ by solving the eikonal equation (White et al., 2020).

We then use the deep learning automatic phase picking algorithm PhaseNet (Zhu & Beroza, 2019) to estimate the probabilities $\nu_{s\phi}(t)$ of P- and S-wave arrivals in continuous seismic data (as illustrated in Figure 3b and Figure S2 in Supporting Information). Next, we shift $\nu_{s\phi}(t)$ according to the computed moveouts and stack the waveform features to identify the most likely source location. This serves as an efficient seismic phase association mechanism (see also Figure 3b). The stacked response, also named beamforming by Frank and Shapiro (2014), is defined as:

$$b_k(t) = \sum_{s \in \mathcal{S}_k} \sum_{\phi \in \{P,S\}} \nu_{s\phi} \left(t + \tau_{sk}^{\phi} \right). \tag{1}$$

Coherent seismic signals produce higher values of $b_k(t)$ when aligned with a likely source k, whereas incoherent noise does not contribute constructively. The set of seismic stations $\mathcal{S}_k$ only considers the ten closest stations to the source k to enhance source-to-station sensitivity. The final source location is determined by identifying the maximum value of the composite network response (CNR) defined as the beamforming maximum over time $\mathcal{B}(t) = \max_k b_k(t)$.

The CNR allows the detection and location of earthquakes with increased sensitivity and precision (Beaucé et al., 2019, 2022, 2024). It provides an initial estimate of the event location by identifying the time at which the beam power reaches its peak. However, the accuracy of this location strongly depends on the grid resolution and the velocity model. A finer grid, with more potential source points k, improves spatial precision but drastically increases computational cost. A key challenge in this process is to distinguish between beams corresponding to real earthquakes and those resulting from noise, unlikely signals, or artifacts. Finally, given the large study area and the heterogeneous station coverage, the stacked signal response varies over time, making the choice of a detection threshold non-trivial. To address this, we implement a dynamic threshold approach based on the cumulative distribution function of the daily CNR. Assuming that most low-amplitude beams do not correspond to real events, we define the threshold at the inflection point, or "knee", of the distribution (Figure 3c). However, in cases where the knee is not well-defined, the uncertainty in event detection could increase. To maintain a conservative yet effective detection criterion, we set the threshold at the 97^{th} percentile of the beam power distribution. We also note that values between the 95^{th} and 99^{th} percentiles can effectively distinguish potential seismic signals while reducing the likelihood of false detections. This adaptive approach ensures that the detection threshold dynamically adjusts to the empirical characteristics of the dataset, optimizing the balance between sensitivity and reliability.

Applying this approach, we detect 130,578 earthquakes during the study period. Each event has P- and S-wave picks from at least five stations, resulting in nearly six million valid picks (about 2.7 million P and 3.1 million S arrivals). Backprojection provides initial locations on the 3D grid described above, and the computations are accelerated on GPUs to keep runtimes practical for this large dataset.

4.2 Event relocation

To improve location accuracy, we relocate all detections with the NonLinLoc-SSST-Coherence algorithm (Lomax, 2001; Lomax et al., 2009; Lomax & Savvaidis, 2022). NonLinLoc uses the P- and S-wave picks previously identified by PhaseNet to perform a grid search and sample the likelihood of hypocenter locations in the regional 3D V_P/V_S velocity model (Figure S3 in the Supplementary Information; Potin et al., 2025). For each of the

130,578 events, it returns an absolute hypocenter and an uncertainty ellipsoid, which form the basis for the subsequent stages.

Then, we apply Source-Specific Station Term (SSST) corrections, which iteratively refine travel-time estimates by minimizing residuals between observed and predicted seismic phase arrivals (Figure S4). This approach accounts for spatial velocity variations, producing smoother station-specific travel-time corrections that adapt to regional heterogeneities, resulting in more precise earthquake locations. However, the S phase residuals show a consistently positive trend across stations (Figure S4), which suggests a systematic bias in the travel time predictions, likely caused by the network geometry. This mainly affects absolute depths and the most distant events, and it is partly mitigated by the coherence relocation, which sharpens relative locations within clusters.

Finally, we apply a relative relocation method based on waveform coherence (Lomax & Savvaidis, 2022), conceptually similar to other techniques such as HypoDD (Waldhauser, 2001) or GrowClust (Trugman & Shearer, 2017), but without relying on differential travel times. High waveform coherence, quantified by the maximum cross-correlation, suggests that close events originate from nearby sources. We stack the location PDFs of highly correlated events and relocate them within their shared probability region. This approach enhances location accuracy, even in regions with sparse station coverage and limited datasets, such as in our case.

The result of this three-step workflow on the catalog is summarized in Figure 4. To allow a direct comparison of how earthquake locations evolve through the workflow, we plot only those events that successfully passed all relocation stages. Out of the initial 130,578 earthquakes, only one event retains its first location, 74,977 events are updated only by the SSST correction, and 55,600 events undergo the full coherence relocation. The median semi major axis of the horizontal uncertainty ellipse is 1.2 , the median semi-minor axis is 0.5 , and the median vertical uncertainty is 1.6 , for all the events. For the maps in Figure 4 we further restrict the plotting to the 49,230 relocated earthquakes with a horizontal uncertainty smaller than 10 . In the outer rise zone (Figure 4a-c) the three panels look very similar, with only minor depth changes, which suggests that the offshore velocity structure and network geometry are still poorly constrained and vertical locations improve only slightly. In contrast, within the red box Figure 4a'-c', which encompasses the Pichilemu fault system, the relocation sharpens the seismicity distribution, with more compact clusters that better align with mapped structures.

4.3 Template matching

Template matching is a technique to identify new earthquakes with a low signal-to-noise ratio from existing templates (Anstey, 1964; Gibbons & Ringdal, 2006; Shelly et al., 2007; Frank & Shapiro, 2014; Skoumal et al., 2014; Beaucé et al., 2018; Cabrera et al., 2021; Beaucé et al., 2022; Minetto et al., 2022). This process quantifies the similarity between seismic waveforms, triggering a new detection when the correlation is sufficiently high (Figure S5). We define as templates a subset of earthquakes whose largest horizontal semi-major axis of the location error ellipse is smaller than 2 . To avoid redundancy, we group highly correlated events and keep, for each group, the one with the smallest combined horizontal and vertical uncertainty. Each template consists of a 10 s window around the picked P wave on the vertical component and the picked S wave on the horizontal components.

We finally cross-correlate the continuous data with the templates in search of coherent signals. New detections are identified when the cross-correlation coefficient exceeds a time-dependent threshold, calculated as 8 times the Root Mean Square (RMS) of each 30 min segment, which is consistent with conservative thresholds used in previous template matching studies (e.g., Shelly et al., 2007; Ross et al., 2019; Beaucé et al., 2022). We require a minimum of three available stations and six channels to trigger a new detection, based on the network-averaged cross-correlation coefficient, and limit the search to a maximum

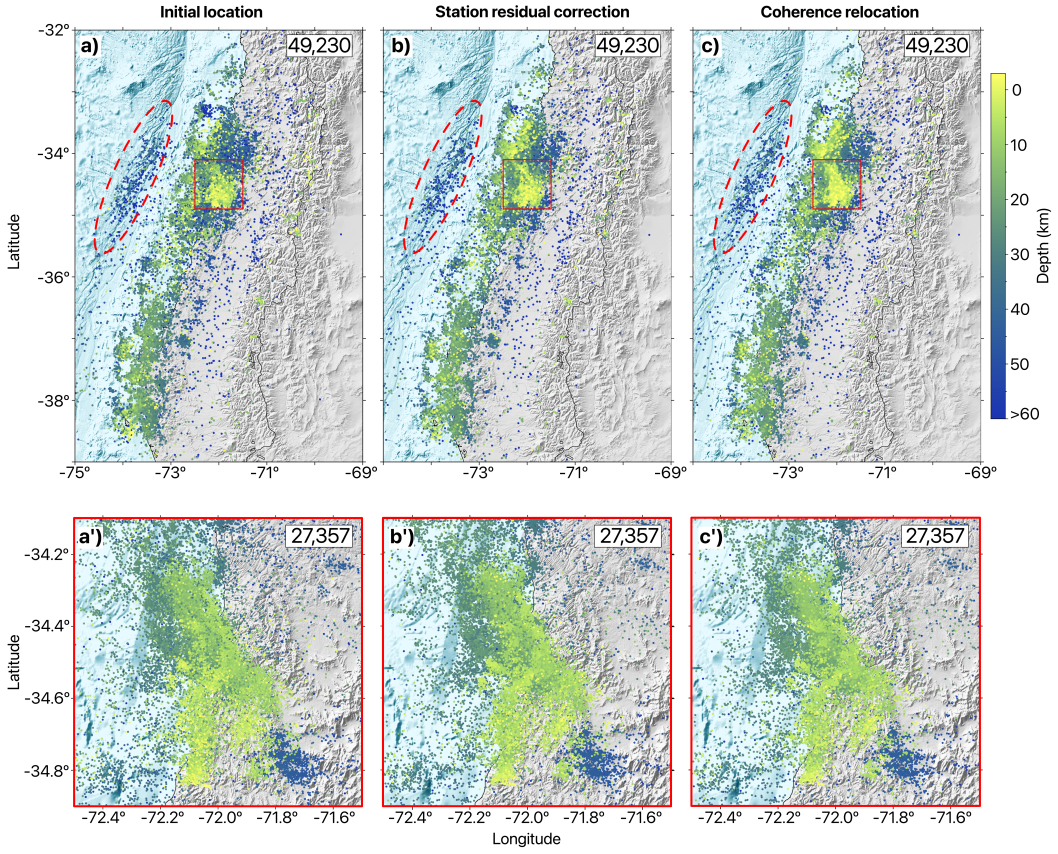

Figure 4. Earthquake locations at different steps of the relocation process. Panels **(a–c)** show the entire study area at different stages of relocation. The dashed red ellipsoid outlines the outer-rise zone, and the red box marks the area of the Pichilemu fault **(a'-c')**. **(a-a')** Initial locations based on automatic picks by PhaseNet. **(b-b')** Time residual corrections between observed picks and theoretical seismic phase arrivals, applied to the entire initial catalog. **(c-c')** Relative relocation based on coherence of nearby seismic signals, which could only be applied to a subset of earthquakes, primarily those near the IMAD network. **(a'–c')** Close-up view of the Pichilemu fault system, an area with a high concentration of aftershocks.

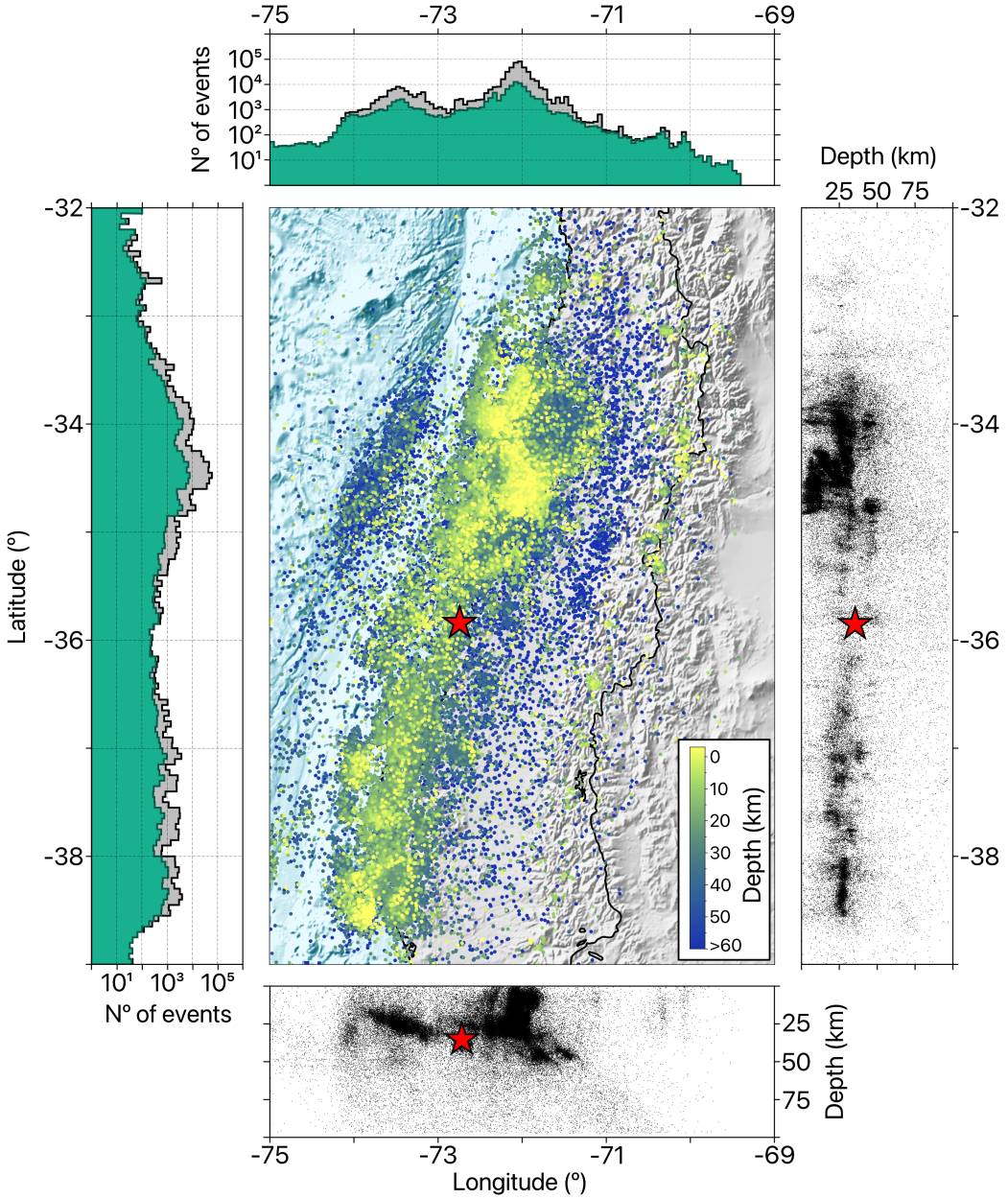

Figure 5. Spatial distribution of the aftershocks in the study area. The central panel corresponds to the final locations of the whole catalog, including the coordinates of the M_w 8.8 mainshock, depicted with a red star and color coded by depth. The top and left panels respectively show the number of earthquakes as a function of longitude and latitude. The green histograms represent the initial catalog, while the grey histograms represent the final catalog after template matching. The right and bottom panels display stacked depth profiles of the earthquake catalog. The bottom panel clearly illustrates subduction across different longitudes, while the right panel shows the concentration of seismicity with latitude as a function of depth. The yellow star marks the location of the mainshock.

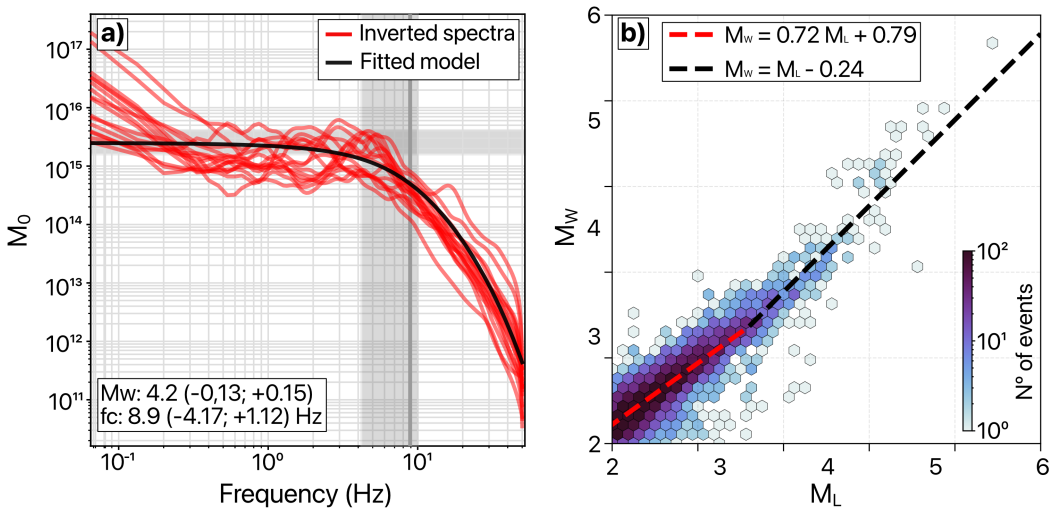

Figure 6. Magnitude estimation method for the earthquake catalog. **(a)** Seismic moment M_0 plotted against the frequency content of the seismic signal for an example event. Red lines show the displacement spectra recorded at different stations for this event, with Brune's model fitted to the stacked spectra (black line). The vertical dark gray rectangle indicates the estimated corner frequency. **(b)** Local magnitude M_L calibration for moment magnitude M_w estimation for nearly 7,000 earthquakes in our catalog, represented by data with low standard deviation values.

of ten stations per template, selected based on proximity, to optimize performance in large seismic networks. For each new detection we assign the hypocenter of its parent template. Template detections therefore densify the catalog and extend the magnitude range, but they do not improve the spatial resolution beyond that of the template set. To ensure that the catalog contains only unique events, we apply a combination of geographic, temporal and similarity based filters. Events that occur within 4 s and 10 of each other are grouped as potential duplicates. Within each group we retain only one event, preferring the detection with the highest template correlation and, when correlations are similar, the one with the smallest location uncertainty. This procedure removes redundant detections while keeping the most reliable representative in each cluster.

From the relocation process, we identify 55,328 well-located earthquakes (with location uncertainties below 2 km) to serve as templates for template matching. To prevent redundant detections caused by highly similar events, we perform a waveform cross-correlation analysis, removing duplicates and retaining 37,990 unique templates. Applying template matching with these events results in the detection of 406,812 new earthquakes, increasing the number of events by a factor 10.7 compared to the starting subset of templates. We assign the locations of these newly detected events to their corresponding parent template, assuming that family members rupture closely spaced sources around the template hypocenter. As shown in the histograms in Figure 5 (top and left panels), the green area represents the initial catalog, while the gray area corresponds to the final catalog after template matching, with bin sizes of 0.1°. Most seismicity is concentrated in the Pichilemu area (34–35°S, 71.5–72.5°W), where we identify the highest density of events both before and after template matching. In practice, the spatial resolution of the catalog is related to the 130,578 initial detected events and relocated with NonLinLoc–SSST–Coherence, while template detections mainly extend the temporal sampling and magnitude range along the same rupture area.

4.4 Magnitude Estimation

To complete our earthquake catalog, we compute the moment magnitude (M_{w}) using the Hanks and Kanamori (1979) equation (see also Table S1 in Supporting Information):

$$M_w = \frac{2}{3}(\log_{10} M_0 - 9.1), \tag{2}$$

where M_0 is the seismic moment, derived from the stacking and fitting of the Brune model (Brune, 1970) to the S-wave displacement spectra recorded by the seismic network (Satriano, 2021). The obtained M_0 values are then integrated into Equation 2 to compute M_{w}. Moment magnitude is advantageous for representing earthquake size, as it does not suffer from saturation and remains reliable across a broad range of seismic events. However, estimating M_{w} for small earthquakes is challenging because their related ground motion is often masked by background noise. Accurate estimation of M_{w} for these minor events relies heavily on the sensitivity of instruments and the density of near-field stations. For the smallest earthquakes, the sampling rate also becomes a limiting factor, because their expected corner frequencies approach or exceed the usable frequency band. In practice, we can only estimate M_0 and M_{w} reliably for events whose spectra are well sampled around the corner frequency.

Therefore, for smaller events or when data quality is insufficient, we estimate M_{w} scaling from local magnitudes (M_L) to homogenize our catalog (Deichmann, 2017). To obtain M_L values for our earthquakes, we first recalibrate the distance-dependent attenuation term in the classical Richter (1935) relation for south-central Chile. This calibration is performed with a joint inversion of amplitude and distance, following the procedure and recommendations of Bormann (2012) and similar regional studies (e.g., Langston et al., 1998; Y.-M. Wu et al., 2005; Condori et al., 2017).

We use 7,119 events with reliable M_w values computed with SourceSpec (Satriano, 2021) as reference magnitudes. These earthquakes span from $M_w \approx 2.0$ to 6.5 and cover hypocentral distances between 10 and 250 km. The inversion includes a soft constraint that keeps the estimated M_L close to M_w for events with small M_w uncertainties, so that the resulting local-magnitude scale remains consistent with the moment-magnitude reference. For each event–station pair, we extract the horizontal waveforms, simulate a Wood–Anderson seismograph, and measure the zero-to-peak displacement amplitude, which we associate with the corresponding reference M_{w} and hypocentral distance.

We describe the distance dependence with a two-term attenuation function that combines geometric spreading and anelastic decay. For each event i and station j we assume

$$\log_{10} A_{ij} = M_{L,i} - a \log_{10}\left(\frac{R_{ij}}{R_{\mathrm{ref}}}\right) - b\,(R_{ij} - R_{\mathrm{ref}}) - S_j, \tag{3}$$

where each amplitude observation A_{ij} is related to the unknown local magnitude $M_{L,i}$, the hypocentral distance R_{ij}, and a station correction S_j.

We solve for all parameters simultaneously using a least squares inversion. The coefficients a and b control the average decay of amplitudes with distance, while S_j represents a static correction that accounts for local site and instrument effects. To avoid trade-offs between the S_j values and the overall magnitude level, we enforce that the network mean of the station terms is zero, which defines a unique reference for the entire network.

We adopt a reference distance of $R_{\mathrm{ref}} = 100$ km, which is commonly used in regional M_L calibrations (Richter, 1935). This value also lies near the center of our sampled distance range. The first term, a, mainly reflects the effective wavefront geometry and average crustal structure, while the second term, b, represents moderate anelastic attenuation. The station terms S_j describe local deviations from the mean amplitude field and are applied directly in the final magnitude equation (Eq. 5) to correct for site-specific amplification.

This approach yields a stable and physically consistent calibration of the local magnitude scale, so we can compute homogeneous M_L values across the network and derive consistent M_{w} estimates for smaller events.

The preferred solution of this inversion corresponds to,

$$a = 1.4209, \qquad b = 0.000736\ km^{-1}, \tag{4}$$

and provides a good fit to the amplitude data. The fit has a mean absolute error of 0.19 magnitude units, a root mean square error of 0.25, and a negligible mean bias in $\log_{10} A$ residuals. This root mean square error corresponds to a standard deviation of about 0.25 magnitude units in the residuals. At the event level, the anchored M_L values differ from M_w^{ref} with a mean absolute difference of 0.20, a root mean square error of 0.30, and a small positive bias of 0.09 in magnitude. These values indicate that the calibrated M_L scale is internally consistent with the observed amplitudes and externally consistent with the reference M_{w}. Once the inversion parameters are fixed, we use the following M_L equation in this study,

$$M_L = \log_{10} A_{WA} + 1.4209\ \log_{10}\left(\frac{R_{\mathrm{hyp}}}{100}\right) + 0.000736\ (R_{\mathrm{hyp}} - 100) + S_j, \tag{5}$$

where A_{WA} is the Wood–Anderson zero to peak displacement amplitude and R_{hyp} is the hypocentral distance in km.

Figure 6a illustrates the stacking of displacement spectra from multiple stations for an earthquake (see also Figure S6 in Supporting Information), which we use to estimate the seismic moment M_0 and derive M_{w} (Equation 2). Based on this information, we calibrate the local magnitude M_L to estimate M_{w} for the entire catalog using the following relationship:

$$M_w \quad = \quad \begin{cases} 0.72M_L + 0.79 & \text{if } M_L \leq 3.6, \\ M_L - 0.24 & \text{otherwise.} \end{cases} \tag{6}$$

These two branches reflect the empirical observation that the scaling between M_L and M_{w} deviates from linearity at low magnitudes (Figure 6b). Following the approach presented by Deichmann (2017), small earthquakes tend to follow a steeper scaling (approximately 1.5:1), while moderate to large events approach a 1:1 relationship. We apply a maximum likelihood bilinear regression and identify a break point at $M_L = 3.6$, although the precise break point may vary between datasets.

This approach homogenizes the catalog magnitude types and delivers M_{w} values ranging from 0.22 to 6.20, with an average of 2.08 and a completeness magnitude M_c of around 1.8. The majority of events cluster at lower magnitudes, with the first quartile at M_{w} 1.83, the median at M_{w} 2.01, and the third quartile at M_{w} 2.25. Approximately 90 of the events have magnitudes below M_{w} 2.61. Periodic spikes in event counts indicate intervals of increased seismicity, which likely correspond to aftershock sequences. Most events fall within the M_{w} 2–3 range, while the larger magnitudes, up to M_{w} 6, are concentrated in the Pichilemu region, which also hosted the two largest aftershocks (M_{w} 7 and 6.9). However, the seismic network became fully operational only a few days after these two events, so they are not included in this catalog.

4.5 Frequency–Magnitude Characteristics and *b*-Value Estimation

We analyze the frequency and distribution of magnitudes across our study area, with the widely applied linear logarithmic relationship (Gutenberg & Richter, 1944)

$$\log_{10} N(\geq M) = a - bM, \tag{7}$$

where $N(\geq M)$ represents the cumulative number of earthquakes with magnitudes greater than or equal to M. The constant a estimates the seismic activity level in the region, while

b indicates the relative proportion of high- to low-magnitude earthquakes, typically near 1. These parameters also serve to determine the catalog's magnitude of completeness M_c defined as the minimum magnitude at which the likelihood of detecting all earthquakes approaches 1. However, this analysis may be biased in cases of periodically low availability of stations or general incompleteness within the dataset (Geffers et al., 2022).

To address the challenges in estimating the b-value, we applied the b-more-incomplete method (Lippiello & Petrillo, 2024), which builds upon the b-positive method (van der Elst, 2021) but improves accuracy by artificially increasing the level of incompleteness in the catalog before estimating b. While the b-positive method calculates b from positive magnitude differences between successive earthquakes, the b-more-incomplete method enhances robustness by filtering out smaller events that could introduce bias due to partial detection. This artificial filtering helps mitigate the effects of short-term aftershock incompleteness (STAI), ensuring that the estimated b-value is less affected by time-dependent variations in detection thresholds and minimizes the effects of overlapping coda waves and sparse network coverage in the catalogs, resulting in a more accurate b-value estimation. In practice, the b-more-incomplete progressively removes the smallest events until the estimated b-value becomes insensitive to further changes in the magnitude threshold. This results in an effective b that is controlled by the better recorded part of the catalog, without relying on the magnitude of completeness.

The temporal variation in the number of available IMAD stations since March 12, 2010, is shown in Figure 7a, together with the daily median location uncertainties of earthquakes. Station availability fluctuates strongly, especially after the first three months, when a gradual decline is observed, with only short week-long recoveries. Toward the end of the period, the number of available stations stabilizes at approximately 15. These fluctuations directly affect earthquake detection and location accuracy, and periods of reduced station coverage coincide with increased location uncertainties (Figure 7a). This effect is also evident in Figure 7b, where regions with dense station coverage (Figure 1b), such as Pichilemu (34 to 35 S), exhibit a higher density of events. Conversely, regions with lower station availability show detection gaps, particularly between 35 to 37 S after about 100 days from the start of the study period. Larger magnitude events are predominantly concentrated at the beginning of the sequence and are mostly related to the Pichilemu area, which further enhances the contrast in detection rates between space and time. As shown in Figure 7c, the magnitude distribution over time highlights a strong concentration of events around M_w 2. The earthquake detection rates (Figure 7c) display the expected decay over time, with occasional swarms that coincide with short-term increases in station availability and local network reactivation. This underlines the strong impact of station coverage on the interpretation of earthquake catalogs. It also highlights the importance of having well located events, since there are periods where template matching could not be applied because of the lack of reliable reference locations, which produces a heterogeneous spatial distribution of new template detections.

We compute the b-value using two different methods, as illustrated in Figure 7d. For this analysis, we use batches of 5,000 earthquakes to estimate the b-value as a function of time. Tests with 3,000 and 7,000 event windows give similar long-term trends, and 5,000 events offer a good compromise between temporal resolution and stability. The black line represents the b-values obtained with the classical maximum likelihood method for events above M_c, while the red line corresponds to estimates from the b-more-incomplete method (Lippiello & Petrillo, 2024). At the beginning of the sequence, the classical b-values fluctuate between about 0.6 and 1.2, then they show a spike up to about 1.6 around day 120, and later fluctuate around 1.2 before tending toward a stable value close to 1.0 at the end of the period. The early values are characteristically low for an aftershock sequence, which likely reflects the limited station coverage and the resulting loss of small events in the catalog. In contrast, the b-more-incomplete estimates show a much more stable behavior over time,

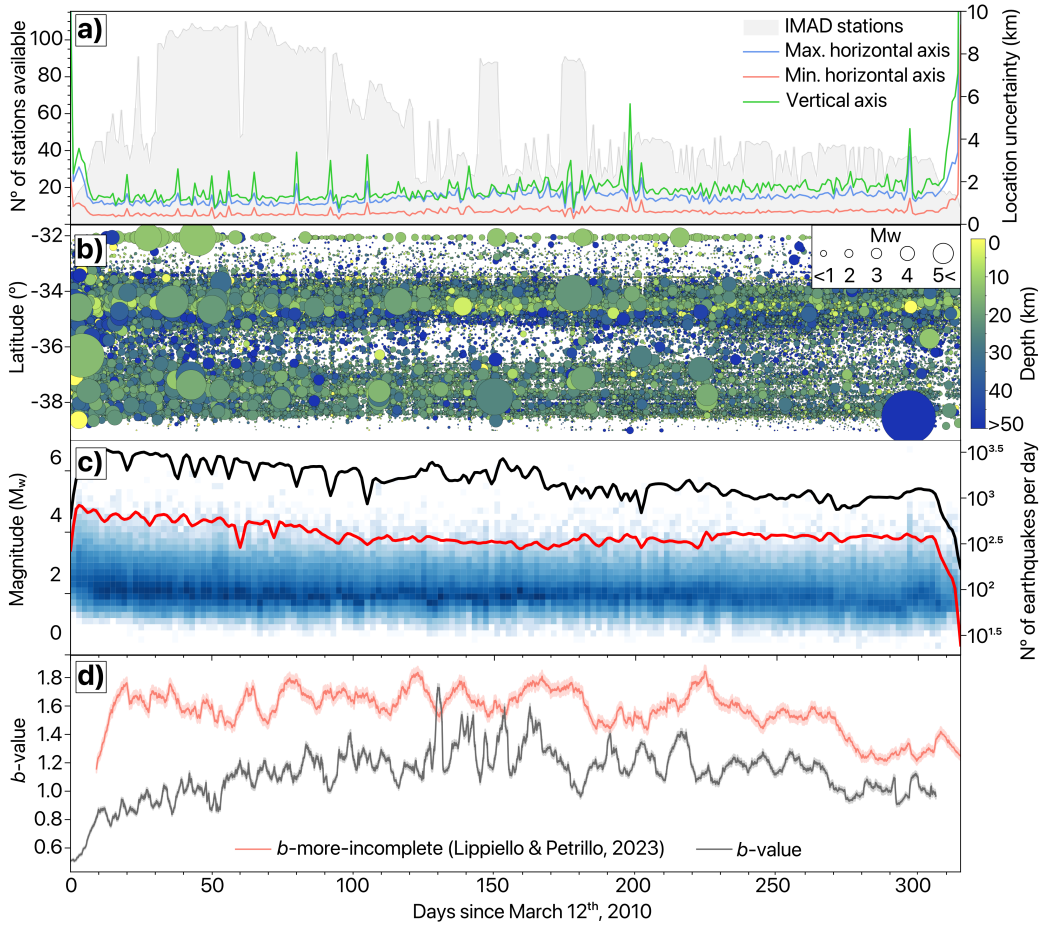

Figure 7. Temporal variations in **(a)** station availability (gray area) and earthquake location uncertainties (colored lines for maximum axis, minimum axis, and depth), **(b)** the spatial distribution in latitude, where circle size represents event magnitude and color indicates depth, **(c)** the magnitude variation in the final catalog (blue squares), and the trends accounting for the number of earthquake detected per day, from the initial catalog (red) and the final catalog (black), and **(d)** the estimated *b*-value using the *b*-more-incomplete method. Shaded areas indicate the uncertainty ranges for both methods. The *b*-more-incomplete method is less sensitive to time-dependent changes in detectability than the classical maximum likelihood estimator.

with values that remain mostly between 1.2 and 1.6 during the first part of the sequence and then converge toward a value close to 1.0 near the end.

Values of b above 1 indicate a relative predominance of smaller earthquakes over larger ones, which is typical for aftershock sequences. The fact that the b-more-incomplete method can be applied to more incomplete catalogs and relies on magnitude increments rather than strict completeness makes it less sensitive to station-dependent variations in detectability. As a result, it provides a more robust description of the temporal evolution of b in this sequence and reduces the impact of changes in station availability on the inferred stress state.

5 Discussion

5.1 Workflow Performance and Limitations

In this study, we employ the BPMF automated detection and location workflow (Beaucé et al., 2024) to build a dense and internally consistent catalog of the Maule aftershock sequence. The workflow performs well across most of the study area, although its effectiveness still depends on the daily station coverage, which remains the main limitation of the Maule network. PhaseNet produced between 6,000 and 12,000 P picks per day on average (maximum around 24,000), and a similar number of S picks, even though the number of available stations changed strongly over time. Nevertheless, the performance decreases for distant offshore events where S-P times exceed 30 s. The sparse and time-variable network further limits detection consistency, especially during periods of strong data gaps.

Within the BPMF workflow, detections rely on the coherence of PhaseNet P and S probability time series across stations rather than on the performance of individual sensors. A real earthquake produces coherent probability increases at consistent moveouts, so even low probabilities sum constructively and generate a clear CNR peak. This makes the detector sensitive to low amplitude events without requiring station-specific thresholds.

Because the Maule network is sparse and highly variable in time, the amplitude of the CNR fluctuates strongly across days. In such conditions, a fixed detection threshold, as used in more stable networks (Beaucé et al., 2019, 2022), would either miss many events on quiet days or admit too many false detections when noise levels are high. Instead, we use a day-dependent threshold based on a high percentile of the daily CNR distribution, typically the 97th percentile (see Section 4.1). This percentile-based threshold keeps the detection performance more homogeneous through the 10-month sequence, at the cost of losing the smallest events on the quietest or noisiest days.

Location accuracy benefits from the regional 3D velocity model (Potin et al., 2025), which improves the coherence of clusters in the central and northern parts of the domain, including the Pichilemu region. The improvement is clear in map view and in cross sections (Figure 10 and Figure S7 in the Supporting Information), where previously diffuse clouds align into narrower structures. However, certain areas remain less well constrained. Offshore events in the outer rise zone and events south of 37 S are affected by reduced station coverage and lower resolution in the velocity model. These locations should be interpreted with caution. Overall, the workflow performs well for a sparse and heterogeneous network, but it does not replace the benefits of a dense permanent array.

The matched filter search is stable in this region. Some station–template correlations can be low (0.2–0.3), but averaging across at least five stations and six channels and applying a median absolute deviation criterion yields robust detections even when individual traces are noisy. This strategy is widely used in BPMF applications (Beaucé et al., 2019, 2022, 2024) and behaves similarly in the Maule dataset. Matched filtering densifies the catalog and lowers the magnitude of completeness, but newly detected events inherit the location of their template. These detections refine the temporal sampling and magnitude range of

the sequence rather than its spatial resolution. The GPU implementation of BPMF makes the backprojection and template matching stages fast and scalable.

Our regional M_L calibration reproduces the reference magnitudes with small bias but still leaves some residual variability. The residuals, shown in Figure S8 in Supporting Information, defined as $M_{\mathrm{ref}} - M_{\mathrm{pred}}$ for each event, are centered near zero and most values lie between about -0.5 and 0.5 magnitude units over distances from 10 to 250 km, with only a few outliers reaching larger absolute values. There is no strong systematic drift with distance, although a mild trend remains at the smallest magnitudes. This suggests that the calibration captures the main attenuation pattern and that the remaining scatter is dominated by unresolved path and site effects, together with measurement noise. When residuals are averaged over several stations per event, they translate into typical M_L uncertainties of about 0.2–0.3 magnitude units. A more detailed study of frequency-dependent Q, κ, and site amplification, using a generalized inversion technique (GIT) to separate source, path, and site contributions on the same dataset, could further reduce this scatter, but this is beyond the scope of the present work. Despite this scatter, the calibrated M_L scale is internally consistent and stabilizes the Mw–M_L relation in the magnitude range most relevant for our aftershock statistics. This internal coherence is what matters for estimating b-values, mapping spatial variations in seismicity, and comparing the behavior of the crust and the subducting slab.

5.2 Comparison with Previous Catalogs

This aftershock sequence has already been the focus of previous studies, resulting in the development of other earthquake catalogs. For instance, Lange et al. (2012) utilized automatic picking methods to compile a catalog of over 20,000 events spanning the first six months of the sequence. Similarly, Rietbrock et al. (2012) applied the STA/LTA triggering method with 2D velocity models, detecting and locating approximately 40,000 earthquakes. While most of their detailed analyses focus on roughly the first two months after the mainshock, the published catalog spans nearly 300 days of seismicity. Additionally, Ryder et al. (2012) produced a catalog using comparable methods, although limited to a shorter period of two and a half months. All these works provided the foundation for our current understanding of the Maule aftershock sequence and were produced with the methods available at the time. They all rely on the same mobile seismic network (IMAD) used in this study. We revisit the same dataset using modern detection and relocation techniques, with the goal of extending the magnitude range, improving location accuracy, and resolving smaller scale structures within the Maule rupture zone.

These catalogs have served as the basis for numerous subsequent studies, including the characterization of afterslip seismic patterns (Agurto et al., 2012) and the development of velocity models through local earthquake tomography, which have revealed new structural features in this segment of the subduction zone (Hicks et al., 2014). Major structures associated with the Maule earthquake rupture, such as those linked to the subduction slab and the crustal portion with high seismic activity near Pichilemu, are well represented in these catalogs (e.g., Ryder et al., 2012) and are consistent in the seismicity distribution. However, the resolution of fine-scale seismic structures has remained limited.

Figure 8 compares the magnitude distribution, temporal evolution, and spatial coverage of seismicity in three catalogs: Rietbrock et al. (2012), the International Seismic Catalog (ISC) (Di Giacomo et al., 2018), and ours, for the same time period. While all catalogs achieve consistent detection completeness for $M_L \geq 3$, our catalog captures a significantly higher number of small-magnitude events ($M_L \leq 2$). This improvement is especially clear during periods of low station coverage, where the adaptive threshold and matched-filter detections maintain stable performance. Our workflow detects 130,578 initial earthquakes and 537,390 total events after template matching, compared with 40,087 events in the catalog of Rietbrock et al. (2012) and 5,261 events in the ISC catalog (Di Giacomo et al., 2018).

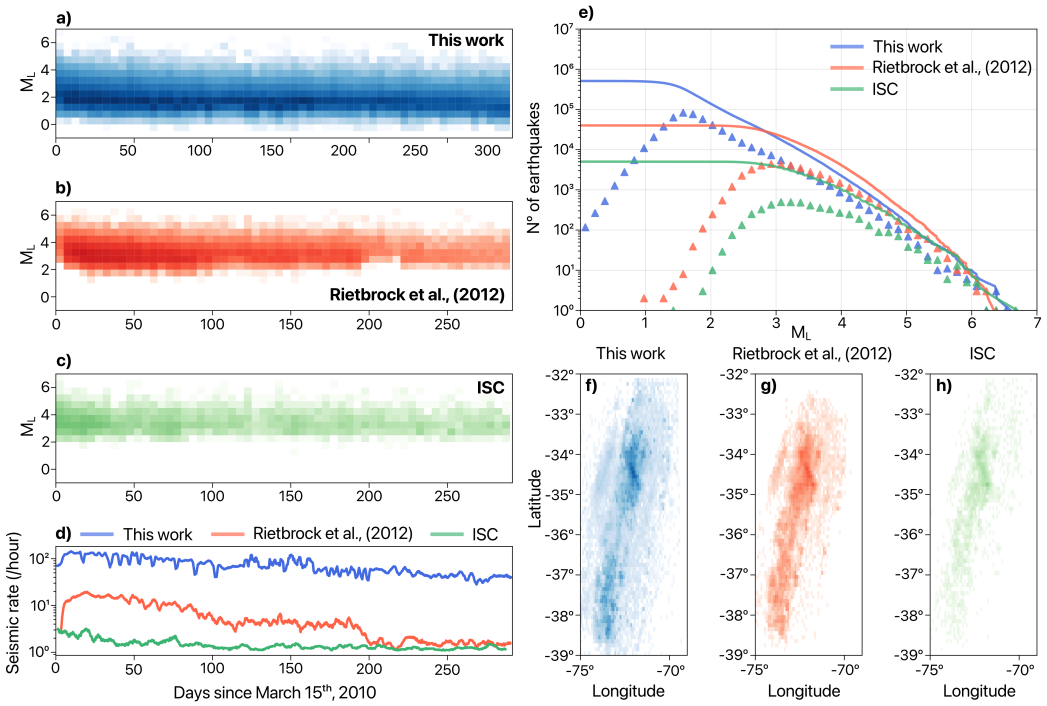

Figure 8. Comparison of three earthquake catalogs based on magnitude distribution, temporal evolution, and spatial coverage for the same period. **(a)**, **(b)**, and **(c)**: 2D histograms showing the distribution of local magnitudes (M_L) over time with bins of 5 days and 0.5 in magnitude. Blue represents the catalog presented in this study, red corresponds to the catalog by Rietbrock et al. (2012), and green denotes the catalog from the ISC (Di Giacomo et al., 2018). Lighter tones indicate lower data density, while darker tones represent higher densities. **(d)**: Seismicity rate (events per hour) over time for the three catalogs, following the same color coding. **(e)**: Magnitude-frequency distribution for the three catalogs. Solid lines represent the cumulative number of events following the Gutenberg–Richter law, while triangles indicate the number of earthquakes for each magnitude bin. **(f)**, **(g)**, and **(h)**: Spatial distribution of seismicity in the rupture zone for each catalog.

This increase reflects the combined effect of improved phase picking and matched filtering. The magnitude of completeness also improves from $M_c \approx 2.7$ in Rietbrock et al. (2012) and above 3.5 in ISC to $M_c \approx 1.8$ in our catalog, which corresponds roughly to a 10-times gain in sensitivity.

The seismicity rate, as shown in Figure 8d, shows similar temporal trends across the three catalogs, but with clear differences in the total number of recorded events. In all three catalogs, short-term drops in rate follow larger earthquakes, when coda waves mask smaller aftershocks. These systematic gaps underscore the need to account for detection limits when interpreting aftershock productivity.

The frequency–magnitude distribution of our catalog, compared to the catalogs of Rietbrock et al. (2012) and the ISC, is presented in Figure 8e. This comparison highlights the improved detection capability of the proposed workflow, which achieves a lower magnitude of completeness by 1 to 2 orders of magnitude, significantly expanding the range of detectable seismic events. Differences in the number of moderate-magnitude events also reflect the fact that each catalog relies on a distinct local–magnitude scale. The Rietbrock et al. (2012) catalog uses a different M_L formulation based on the methods available at the time, while our study recalibrates a regional attenuation model directly from the Maule dataset. Because the ISC catalog relies on a low-density permanent network, it detects fewer events across all magnitude ranges.

Figure 8f–h show that the overall shape of the seismicity distribution is consistent between catalogs, with a pronounced concentration around the Pichilemu region. Overall, our catalog reveals additional small-scale structures and secondary clusters, particularly in the Pichilemu fault area and in the central part of the rupture. In Pichilemu, aftershocks cluster more tightly along narrow NNW-striking structures and secondary NE-trending branches than in previous Maule catalogs. In Figure S7, we compare our locations with those of Rietbrock et al. (2012) using identical map views and cross sections. The tighter clusters and improved spatial coherence highlight the gains from combining increased completeness with a 3D velocity model and successive relocation stages (see Text S1 and Figure S7 in the Supporting Information). This improved resolution, together with the regional M_L calibration, allows us to map spatial and temporal b-value variations that were not resolved in earlier work. These improvements are most robust in regions with dense station coverage and good velocity control, whereas offshore and southern areas remain less well constrained and should be interpreted carefully.

We successfully re-detect approximately 88 % of the events reported by Rietbrock et al. (2012) and 90 % of those cataloged by the Centro Nacional de Sismología de Chile (CSN) and the ISC (Di Giacomo et al., 2018). Events not recovered usually correspond to signals with too few picks to meet the internal consistency criteria of our workflow. Excluding them keeps the catalog homogeneous and avoids introducing poorly constrained detections.

5.3 Geotectonic Implications

This catalog provides a detailed and consistent view of the aftershock sequence of the 2010 Maule earthquake and shows how different structural domains responded to the mainshock. The most intense postseismic activity occurs in the Pichilemu area (Figure 9, B-B' and Figure 10), where a shallow normal fault system accommodates upper crustal extension above the main slip patch. The normal-faulting nature of this system and its potential reactivation within the area of highest coseismic slip have been already well documented (Farías et al., 2011; Lange et al., 2012; Ryder et al., 2012; Lieser et al., 2014). Using the increased number of small earthquakes, we refine the view of the Pichilemu fault system in Figure 10. Seismicity related to this fault system was isolated using HDBSCAN, a hierarchical density-based algorithm (Campello et al., 2013), often used to distinguish earthquake patterns within catalogs (Essing & Poli, 2024). The clustering was applied in four dimensions considering location coordinates and origin time.

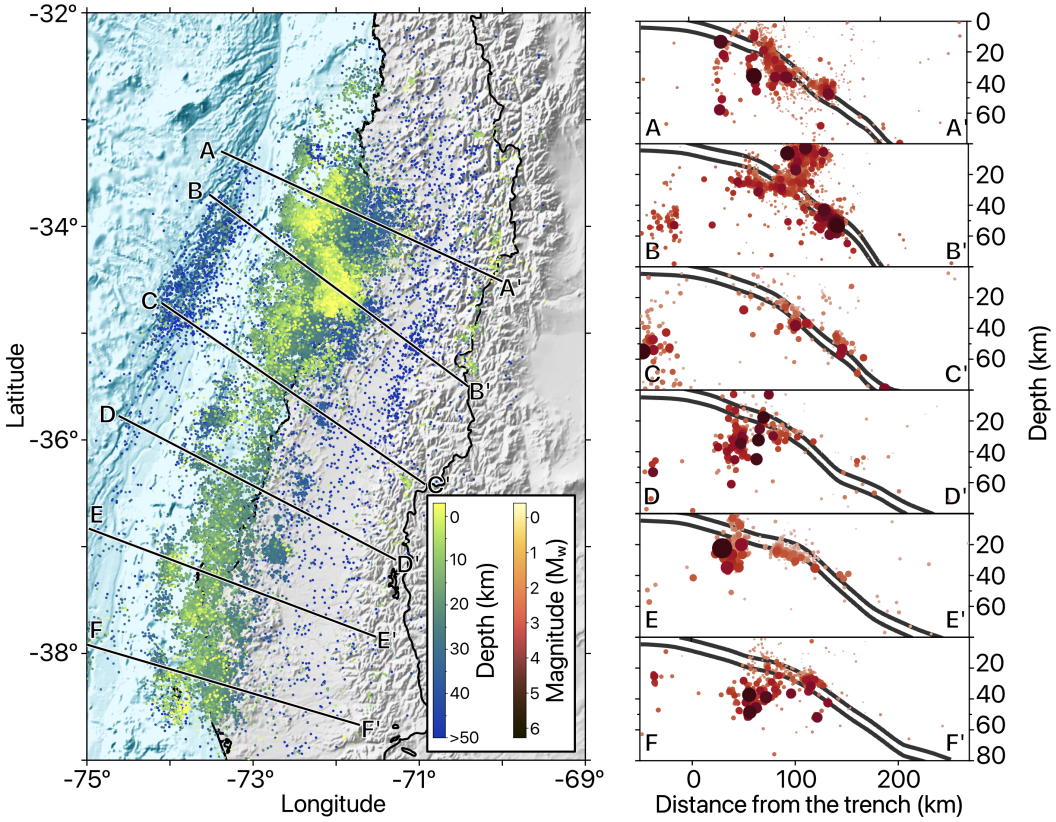

Figure 9. Spatial distribution of seismicity (colored dots) and profiles perpendicular to the subduction trench (black lines, A-F). On the left panel, color represents depth, while in the cross-sections on the right (A-F), color indicates magnitude. Black lines in the cross-sections correspond to the slab model (Slab 2.0, Hayes et al., 2018) for the subduction zone in this region.

In this area, we observe a main normal fault characterized by an azimuth–dip orientation of N40 W/S30 W and extending for about 49 (Figure 10, A–A'). The fault system shows distinct seismic patterns, with branches approximately perpendicular to the main structure and forming an L-shaped distribution. Seismicity is concentrated between 5 and 20 depth along these intersecting faults, defining a seismogenic thickness of roughly 5 km and a distributed deformation field around the main fault.

This configuration points to a conjugate normal-fault system, where secondary NE–SW structures intersect the main NW–SE fault. The geometry is typical of upper-plate extensional regimes along the Chilean margin (e.g., J. A. Ruiz et al., 2014; Piquer et al., 2019; Santibáñez et al., 2019) and is consistent with seismological models of the largest 2010 M_w 7.0–M_w 6.9 aftershocks in the area (J. A. Ruiz et al., 2014). Comparable conjugate fault patterns have been described in other complex normal-faulting sequences, such as the M_w 6.5 Ludian earthquake (Li et al., 2024) and the M_w 7.1 Ridgecrest earthquake (Liu et al., 2019), supporting an interpretation in terms of localized crustal stretching and stress transfer within the upper plate. Altogether, the seismicity distribution offers a coherent and high-resolution seismological image of the Pichilemu fault system and provides new constraints on its geometry and on the mechanisms of upper-plate fault reactivation in central Chile.

Offshore Pichilemu, we also observe clear seismic activity in the outer-rise zone. This finding aligns with previous studies, which suggest that this seismicity is a direct response to the high coseismic slip in the region, potentially resulting from the activation of shallow normal fault systems under extensional forces following large slip events (Moscoso & Contreras-Reyes, 2012; Lange et al., 2012; Rietbrock et al., 2012; J. A. Ruiz & Contreras-Reyes, 2015). Several events appear near or below 30 depth. These values should be interpreted with caution because long travel paths and possible mixing between direct and reflected phases can affect depth estimates in this offshore region.

Seismic activity associated with the subducting slab is present throughout the rupture zone. Notably, two distinct bands of seismicity are observed along the profiles: one at depths of 20 km to 35 km (Figure 9, A–F) and another, deeper band at approximately 50 km, primarily in Figure 9, A–C. A horizontal gap in seismicity is evident in the region closest to the mainshock (Figure 5), suggesting minimal post-mainshock activity in this area, likely due to significant coseismic stress release. While some seismicity does not align precisely with the slab model, it follows a consistent depth distribution, highlighting distinct tectonic behaviors captured by this catalog.

A marked decrease in aftershock activity is observed around 36°S, near the mainshock hypocenter, forming a distinct low-seismicity zone within the rupture area (Figures 9 and 5). South of this region, toward Concepción, the sequence shows sparse and discontinuous seismicity, with small clusters separated by aseismic patches (Figure 9). This quiescence is consistent with substantial coseismic stress release and a limited postseismic response in the southern segment. The scarcity of shallow or interface events emphasizes the along-strike segmentation of deformation and the heterogeneous reactivation of the plate interface following the Maule earthquake. Overall, these patterns outline how the crustal faulting system, the outer-rise region, and the slab responded to stress redistribution after the Maule earthquake.

5.4 Spatial Patterns of Seismicity and *b*-Value Variations

The *b*-value provides a simple way to follow how stress and structure vary across the rupture zone, being linked to fault coupling, stress regime, and fluid content (Custódio & Archuleta, 2006; Chiba, 2019; Folesky, 2024; Collettini & Tinti, 2025). We estimate it using two approaches, the classical maximum likelihood method (Aki, 1965) and the *b*-more-incomplete method (Lippiello & Petrillo, 2024), which reduces the impact of time-variable completeness. The classical estimate starts with unusually low values (0.6–1.2) during the

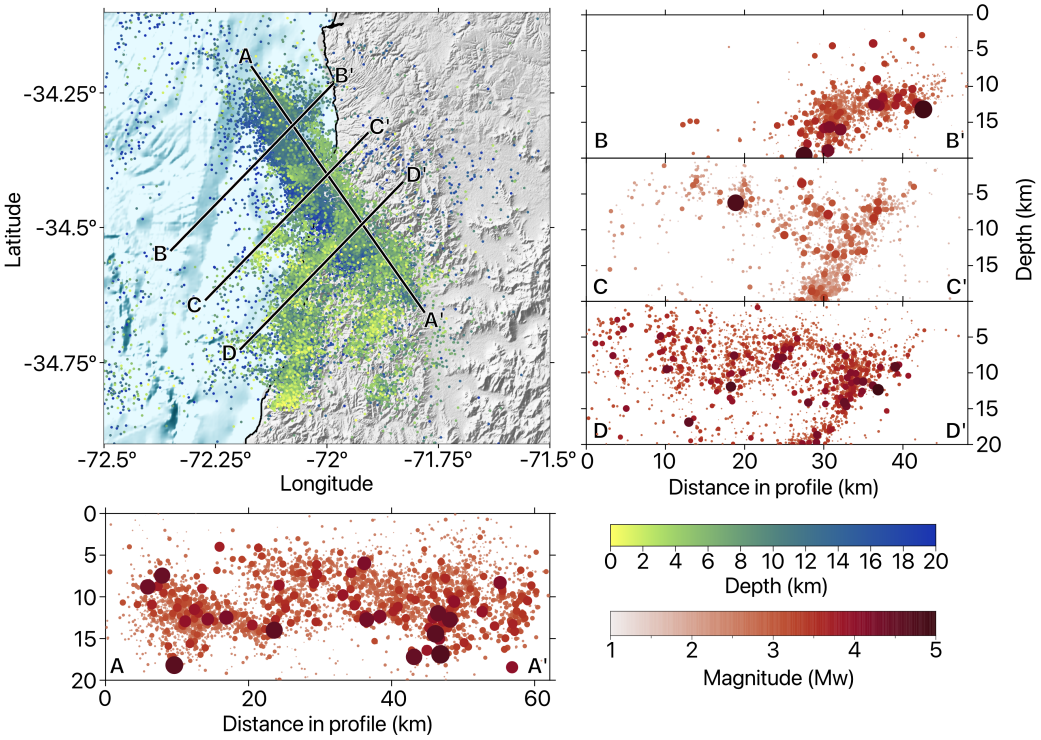

Figure 10. Spatial evolution of the Pichilemu fault system. Earthquakes are shown as dots color-coded by depth in the latitude-longitude map, and by the estimated moment magnitude (M_w) in the cross-sections. Profiles along the black lines (A-D) include one in the main Pichilemu fault's azimuthal direction (A-A') and three perpendicular sections (B-D). The cross-sections illustrate the southwest dip direction of the northwest-trending fault and a series of conjugate faults, forming an L-shaped faulting system.

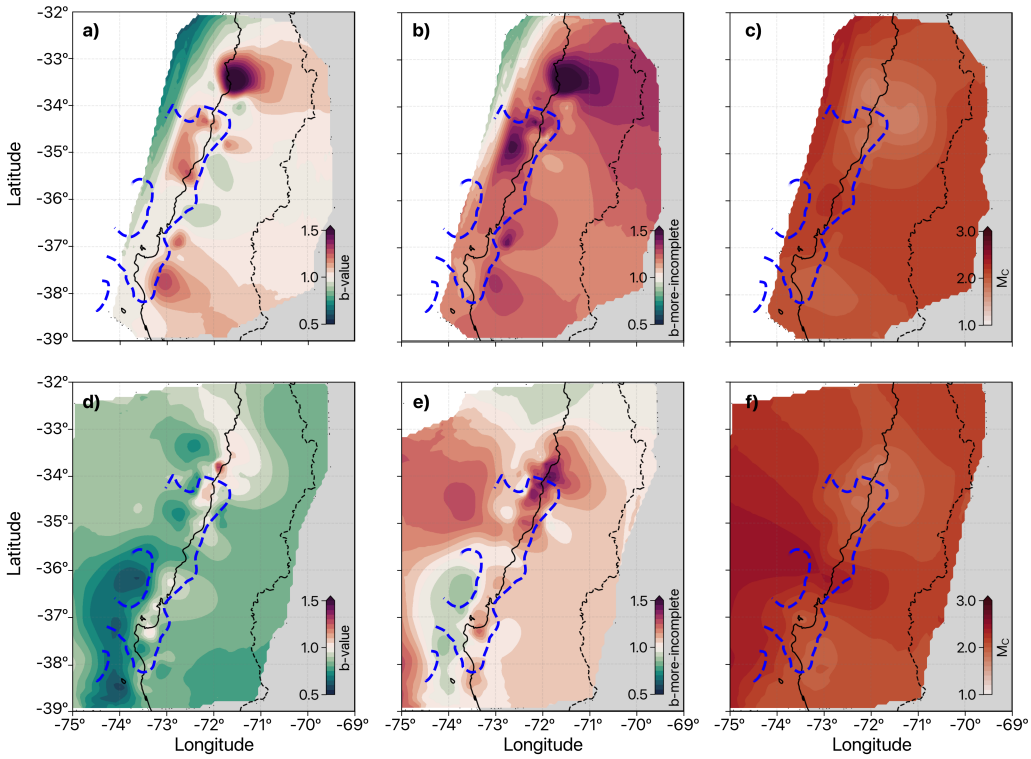

Figure 11. Spatial distribution of the b-value and M_c. We compute these values within earthquake clusters of at least 200 events. **(a–c)** Crustal seismicity. **(d–f)** Slab-related seismicity. Columns show the classical b-value, the b-more-incomplete estimate, and the corresponding M_c. The dashed blue line marks the 5 m coseismic slip contour from the model of Yue et al. (2014); regions inside the contour correspond to slip values exceeding 5 m.

first weeks, rises sharply to $\sim$ 1.6 around day 120, and then stabilizes near 1.0 toward the end of the period (Figure 7d). In contrast, the b-more-incomplete remains much more stable, mostly between 1.2 and 1.6 during the first months, and gradually converges toward a value close to 1.0. These differences are closely linked to the evolution of station availability. As shown in Figure 7a, the number of IMAD stations decreases from more than 80 at the start to about 15 at the end of the study period, which affects detectability. As a result, the classical method drops to 0.6–0.8, while the b-more-incomplete remains stable at 1.2–1.6, as it is less sensitive to short-term aftershock incompleteness and variable detection thresholds.

To map spatial variations (Figure 11), we follow an iterative clustering strategy (Hartigan, 1975). For each of the $N = 100$ iterations, we randomly select a number of clusters k between 50 and 500 and obtain them using mini-batch k-means (Sculley, 2010; J. Wu, 2012). This produces clusters of variable size, with a typical target of about 400 events per cluster. Clusters with fewer than 200 events are discarded to ensure stable statistics. For every iteration, we estimate M_c, the classical b-value (Aki, 1965), and the b-more-incomplete (Lippiello & Petrillo, 2024) within each remaining cluster, assign these values to all earthquakes in that iteration, and repeat the workflow. The final maps represent the average of all 100 iterations, which smooths out random cluster boundaries and yields stable spatial patterns. We avoid interpreting clusters where M_c is high, since these areas are more sensitive to detection biases. Given the magnitude uncertainties and the finite number of events per cluster, we do not treat b-value differences smaller than about 0.2 as significant and focus instead on robust, large-scale patterns that are stable across different window sizes and

random cluster realizations. The gridded fields are obtained by interpolating the averaged cluster values onto a regular latitude–longitude grid.

Figure 11 illustrates the spatial variability of the b-value and the corresponding magnitude of completeness M_c for crustal (a–c) and slab-related (d–f) seismicity. For crustal events, the classical b-value map (Figure 11a) shows values close to 1.0 along most of the rupture, increasing to about 1.3 around Pichilemu and in parts of the southern segment, and exceeding 1.5 in the northern onshore area where anthropogenic sources (e.g., copper mining) and numerous small, shallow events are present. We therefore interpret much of this high-b patch as non-tectonic in origin. The b-more-incomplete estimates (Figure 11b) retain the first-order along-strike pattern but appear smoother and less sensitive to local variations in M_c. The crustal M_c map (Figure 11c) ranges from about 1.5 to 3.0, with higher values offshore and in areas of sparse station coverage, and correlates strongly with the spatial variability of the classical b-value. This correlation indicates that part of the spatial variability in the classical b-value map reflects completeness changes rather than genuine changes in the magnitude–frequency distribution.

For slab-related seismicity, classical b-values (Figure 11d) are generally lower, ranging from 0.5 to 1.0 beneath the southern segment and up to approximately 1.3 beneath Pichilemu, again following the main patterns in M_c. In contrast, the slab b-more-incomplete map (Figure 11e) reveals a clearer along-strike segmentation, with higher b-values in the northern part of the rupture and values close to 1.0 in the south. The slab M_c distribution (Figure 11f) is similar, with higher values where station coverage is sparse. Together, these maps indicate that classical b-values are strongly influenced by spatial variations in M_c, whereas the b-more-incomplete estimates provide a more stable and less completeness-biased representation of the underlying crustal and slab segmentation.

These spatially variable and temporally evolving b-values are consistent with the idea that earthquake magnitude distributions reflect a dynamically evolving stress field and structural heterogeneity (Herrmann et al., 2022). Taken together, the b-more-incomplete estimates highlight a pronounced along-strike contrast in b-value for crustal earthquakes, with the highest b-values in the northern segment ($\sim$33 to 35 S) and lower b-values in the southern segment ($\sim$36 to 38 S). We interpret this contrast as consistent with a weaker, fluid-influenced plate interface in the north, where elevated pore fluid pressure (p_f) tends to reduce the effective normal stress ($\sigma_\mathrm{eff} = \sigma_\mathrm{n} - p_\mathrm{f}$) and favors a higher proportion of small to moderate earthquakes (Schorlemmer et al., 2005; Scholz, 2015). In contrast, the lower b-values in the south are compatible with a relatively drier, more strongly coupled interface and a less fractured upper plate, characterized by lower pore fluid pressure and persistently high σ_eff. Classical b-value estimates remain more sensitive to spatial variations in M_c, whereas the b-more-incomplete estimates provide a more robust and less completeness-biased view of this segmentation.

Other factors, such as heterogeneous path and site effects or local variations in magnitude uncertainty, may also contribute to the observed patterns. This first-order north–south contrast is, however, consistent with previous interpretations of fluid-rich versus mechanically stronger domains derived from geodetic, structural, and b-value analyses (Tassara et al., 2016; Arroyo-Solórzano & Linkimer, 2021), and is compatible with scenarios in which fluids released from the dehydrating Nazca slab accumulate and are redistributed along the plate interface. The strongest b-value gradients occur adjacent to the regions of highest coseismic slip (Yue et al., 2014), consistent with stress concentration near the edges of the main slip patches. Together, these patterns support a segmented view of the Maule rupture and reflect the redistribution of stress, and possibly pore fluid pressure, after the M_w 8.8 earthquake.

6 Conclusions

This study presents a high-resolution catalog of the aftershock sequence of the 2010 M_w 8.8 Maule earthquake in south-central Chile, covering the period from March 2010 to January 2011. By reanalyzing data from the IMAD seismic network with a workflow that combines deep-learning-based detection method with relative relocation and template matching, we identify 537,390 earthquakes, about 13 times more events than reported in previous studies. The catalog spans magnitudes from M_w 0.2 to M_w 6.2, reaches a completeness level of about M_w 1.8, and resolves fine-scale seismic structures along the rupture zone, particularly in the Pichilemu region.

The two estimation methods reveal markedly different temporal evolutions of the b-value. The b-more-incomplete approach yields consistently high values throughout most of the sequence, whereas the classical maximum likelihood estimate starts from low values and increases with time. Despite these contrasting trends, both methods converge toward $b \sim 1$ after roughly 270 days. This apparent stabilization may reflect a progressive transition toward a more mature aftershock regime. However, the concurrent loss of seismic stations during the later stages introduces uncertainty as to whether this trend represents a genuine physical process or an artifact of decreasing detection capability.

Spatially, the catalog reveals a clear along-strike segmentation of b-values. Higher b-values in the northern segment and lower values in the southern segment are consistent with along-strike variations in effective normal stress, $\sigma_{\mathrm{eff}} = \sigma_{\mathrm{n}} - p_{\mathrm{f}}$. Elevated pore-fluid pressure in the north likely reduces σ_{eff}, promoting a higher proportion of small to moderate earthquakes, whereas lower b-values in the south are consistent with a relatively dry, more strongly coupled plate interface and a less fractured upper plate. Taken together with previous geodetic and structural studies that document two main high-slip regions and long-term forearc segmentation along the Maule margin (Moreno et al., 2010; Jara-Munoz et al., 2015; Tassara et al., 2016), these contrasts suggest that along-strike variations in stress, fluid pressure, and inherited structure exert a first-order control on the postseismic evolution of the sequence.

This catalog provides a detailed and internally consistent dataset that enables future investigations of key physical processes governing the rupture potential and dynamic evolution of seismicity in subduction margins. It offers opportunities to correlate seismic observations with geodetic models (e.g., afterslip, coupling maps) and to better constrain earthquake parameters (e.g., source contribution, attenuation parameters, site effects). In this study, we apply this workflow to a large aftershock sequence and demonstrate that it is effective and can be used in other tectonic settings with variable data coverage and network configurations.

Data Availability Statement

The complete earthquake catalog is provided both in the Supporting Information and in the Zenodo repository described by Flores-Allende et al. (2025) (`https://doi.org/10.5281/zenodo.17858890`). The Supporting Information provides complementary material related to the workflow, while the Zenodo repository contains the Python scripts together with detailed instructions on how to reproduce the workflow. Seismic waveform data were accessed online from the contributing seismic networks, and all records remain publicly available through their corresponding data centers. The IMAD network (Beck et al., 2014) includes the FDSN code XS (Vilotte et al., 2011), operated by CNRS-INSU and IRIS/PASSCAL, with data publicly available at the RESIF data center (`https://doi.org/10.15778/RESIF.XS2010`). The FDSN code XY (Steve Roecker & Ray Russo, 2010) was operated by GEF/SeisUK, and its data are accessible through the IRIS data center (`https://www.iris.edu/hq/`). The 3A network, also operated by GEF/SeisUK, is available via IRIS.

The ZE network, provided by GIPP (GFZ), can be accessed through the GEOFON data center (`https://geofon.gfz.de/waveform/archive/network.php?ncode=ZE&year=2010`).

All algorithms used in this study are open source and publicly available. The BackProjection and Matched Filter (BPMF) workflow (Beaucé et al., 2024) is accessible at `https://github.com/ebeauce/Seismic_BPMF`. The NonLinLoc-SSST-Coherence algorithm (Lomax & Savvaidis, 2022) is available at `http://alomax.free.fr/nlloc/` and through Zenodo (`https://zenodo.org/records/13693145`). SourceSpec (Satriano, 2021) can be found at `https://github.com/SeismicSource/sourcespec`, and the implementation of b-value estimation methods (Lippiello & Petrillo, 2024) is provided at `https://github.com/caccioppoli/$b$-more-positive`.

All computations were performed using Python version 3.11.11 (Van Rossum et al., 2007) (`https://www.python.org/`). The main scientific libraries used are ObsPy 1.4.2 (Beyreuther et al., 2010) for waveform retrieval and preprocessing (`https://doi.org/10.5281/zenodo.15309143`); SciPy 1.13.0 (Virtanen et al., 2020) for optimization and interpolation (`https://scipy.org/`); and Scikit-learn 1.6.1 (Pedregosa et al., 2011) for data analysis, including clustering with HDBSCAN (McInnes et al., 2017) and MiniBatch K-means (J. Wu, 2012) (`https://scikit-learn.org/stable/`). Figures were created using Matplotlib 3.10.1 (Hunter, 2007) (`https://matplotlib.org/`), and maps were produced with PyGMT (Wessel et al., 2019; Uieda et al., 2021) (`https://www.generic mapping-tools.org/`) and Cartopy 0.24.1 (Met Office, 2015) (`https://scitools.org.uk/cartopy/docs/latest/`).).

Conflict of Interest Statement

The authors have no conflicts of interest to disclose.

Acknowledgments

This work was funded through the ANR-22-CPJ1-0020-01 program. E. Beaucé was funded by the Brinson Foundation. L.F. Bonilla was funded by project ANR E-City, AAPG 2021 – CES 22. Continuous seismic data were provided thanks to the collaborative efforts of IRIS, IPGP, ENS, and GFZ. Numerical computations were conducted on the S-CAPAD/DANTE platform at IPGP, France. We sincerely thank Sergio Ruiz and Raúl Madariaga for their valuable discussions on seismicity in the Maule region. We also acknowledge Javier Ojeda, Leoncio Cabrera, and Martin Vallée for their insightful contributions to discussions on seismic parameters relevant to this study. Additionally, we extend our appreciation to Antony Lomax, Jannes Münchmeyer, and Bertrand Potin for their constructive feedback on the event relocation process. We also thank the Andes-FrenSZ collaboration research program and associated researchers for their valuable comments and contributions. Finally, we are grateful to all researchers at IPGP, Universidad de Chile, and ISTerre who provided thoughtful insights, discussions, and feedback that contributed to improving this study. We are very thankful to the journal editor Rachel Abercrombie, the associate editor and three anonymous reviewers for their constructive comments and suggestions that significantly improved the quality and clarity of this work.

References

Agurto, H., Rietbrock, A., Ryder, I., & Miller, M. (2012). Seismic-afterslip characterization of the 2010 mw 8.8 maule, chile, earthquake based on moment tensor inversion. *Geophysical Research Letters*, *39*(20).

Aki, K. (1965). Maximum likelihood estimate of b in the formula log n= a-bm and its confidence limits. *Bull. Earthquake Res. Inst., Tokyo Univ.*, *43*, 237–239.

Allen, R. (1982). Automatic phase pickers: Their present use and future prospects. *Bulletin of the Seismological Society of America*, *72*(6B), S225–S242.

Anstey, N. A. (1964). Correlation techniques–a review. *Geophysical Prospecting*, *12*(4), 355–382.

Aron, F., Cembrano, J., Astudillo, F., Allmendinger, R. W., & Arancibia, G. (2015). Constructing forearc architecture over megathrust seismic cycles: Geological snapshots from the maule earthquake region, chile. *Bulletin*, *127*(3-4), 464–479.

Arroyo-Solórzano, M., & Linkimer, L. (2021). Spatial variability of the b-value and seismic potential in costa rica. *Tectonophysics*, *814*, 228951.

Båth, M. (1965). Lateral inhomogeneities of the upper mantle. *Tectonophysics*, *2*(6), 483–514.

Beaucé, E., Frank, W. B., Paul, A., Campillo, M., & van Der Hilst, R. D. (2019). Systematic detection of clustered seismicity beneath the southwestern alps. *Journal of Geophysical Research: Solid Earth*, *124*(11), 11531–11548.

Beaucé, E., Frank, W. B., & Romanenko, A. (2018). Fast matched filter (fmf): An efficient seismic matched-filter search for both cpu and gpu architectures. *Seismological Research Letters*, *89*(1), 165–172.

Beaucé, E., Frank, W. B., Seydoux, L., Poli, P., Groebner, N., van der Hilst, R. D., & Campillo, M. (2024). Bpmf: A backprojection and matched-filtering workflow for automated earthquake detection and location. *Seismological Research Letters*, *95*(2A), 1030–1042. Retrieved from `https://zenodo.org/records/14838292` ([Software]) doi: 10.5281/zenodo.14838292

Beaucé, E., van der Hilst, R. D., & Campillo, M. (2022). Microseismic constraints on the mechanical state of the north anatolian fault zone 13 years after the 1999 m7. 4 izmit earthquake. *Journal of Geophysical Research: Solid Earth*, *127*(9), e2022JB024416.

Beck, S., Rietbrock, A., Tilmann, F., Barrientos, S., Meltzer, A., Oncken, O., ... Russo, R. M. (2014). Advancing subduction zone science after a big quake. *Eos, Transactions American Geophysical Union*, *95*(23), 193–194. ([Dataset])

Beyreuther, M., Barsch, R., Krischer, L., Megies, T., Behr, Y., & Wassermann, J. (2010). Obspy: A python toolbox for seismology. *Seismological Research Letters*, *81*(3), 530–533. Retrieved from `https://zenodo.org/records/15309143` ([Software]) doi: 10.5281/zenodo.15309143

Bilek, S. L., & Lay, T. (2018). Subduction zone megathrust earthquakes. *Geosphere*, *14*(4), 1468–1500.

Bormann, P. (2012). Magnitude calibration formulas and tables, comments on their use and complementary data. *New Manual of Seismological Observatory Practice 2 (NMSOP-2)*, 1–19. Retrieved from `https://doi.org/10.2312/GFZ.NMSOP-2_DS_3.1` (In: Bormann, P. (Ed.), *New Manual of Seismological Observatory Practice 2 (NMSOP-2)*) doi: 10.2312/GFZ.NMSOP-2_DS_3.1

Brune, J. N. (1970). Tectonic stress and the spectra of seismic shear waves from earthquakes. *Journal of geophysical research*, *75*(26), 4997–5009.

Cabrera, L., Ruiz, S., Poli, P., Contreras-Reyes, E., Osses, A., & Mancini, R. (2021). Northern chile intermediate-depth earthquakes controlled by plate hydration. *Geophysical Journal International*, *226*(1), 78–90.

Campello, R. J., Moulavi, D., & Sander, J. (2013). Density-based clustering based on hierarchical density estimates. In *Pacific-asia conference on knowledge discovery and data mining* (pp. 160–172).

Campos, J., Hatzfeld, D., Madariaga, R., López, G., Kausel, E., Zollo, A., ... Lyon-Caen, H. (2002). A seismological study of the 1835 seismic gap in south-central chile. *Physics of the Earth and Planetary Interiors*, *132*(1-3), 177–195.

Chiba, K. (2019). Spatial and temporal distributions of b-values related to long-term slow-slip and low-frequency earthquakes in the bungo channel and hyuga-nada regions, japan. *Tectonophysics*, *757*, 1–9.

Collettini, C., & Tinti, E. (2025). The influence of lithology and fault source volume on the magnitude–frequency-distribution of earthquakes. *Geophysical Research Letters*,

52(2), e2024GL110354.

Condori, C., Tavera, H., Marotta, G. S., Rocha, M. P., & França, G. S. (2017). Calibration of the local magnitude scale (ml) for peru. *Journal of Seismology*, *21*(4), 987–999.

Custódio, S., & Archuleta, R. (2006). b-values as a proxy for stress–inferences for dynamic modeling of the 2004 parkfield earthquake. *EOS Trans. AGU, 87 (52), Fall Meet. Suppl., Abstract S23C*, *167*.

Deichmann, N. (2017). Theoretical basis for the observed break in ml/m w scaling between small and large earthquakes. *Bulletin of the Seismological Society of America*, *107*(2), 505–520.

Delouis, B., Nocquet, J.-M., & Vallée, M. (2010). Slip distribution of the february 27, 2010 mw= 8.8 maule earthquake, central chile, from static and high-rate gps, insar, and broadband teleseismic data. *Geophysical Research Letters*, *37*(17).

Di Giacomo, D., Engdahl, E. R., & Storchak, D. A. (2018). The isc-gem earthquake catalogue (1904–2014): status after the extension project. *Earth System Science Data*, *10*(4), 1877–1899.

Essing, D., & Poli, P. (2024). Unraveling earthquake clusters composing the 2014 alto tiberina earthquake swarm via unsupervised learning. *Journal of Geophysical Research: Solid Earth*, *129*(1), e2022JB026237.

Farge, G., & Brodsky, E. E. (2025). The big impact of small quakes on tectonic tremor synchronization. *Science Advances*, *11*(20), eadu7173.

Farías, M., Comte, D., Roecker, S., Carrizo, D., & Pardo, M. (2011). Crustal extensional faulting triggered by the 2010 chilean earthquake: The pichilemu seismic sequence. *Tectonics*, *30*(6).

Felzer, K. R., Abercrombie, R. E., & Ekstrom, G. (2004). A common origin for aftershocks, foreshocks, and multiplets. *Bulletin of the Seismological Society of America*, *94*(1), 88–98.

Flores-Allende, R., Seydoux, L., Beauce, E., Bonilla, L.-F., Guéguen, P., & Satriano, C. (2025). *Repository for mw 8.8 maule aftershock deep-learning-based catalog.* Dataset. Zenodo. Retrieved from `https://doi.org/10.5281/zenodo.17858890` doi: 10.5281/zenodo.17858890

Folesky, J. (2024). Different earthquake nucleation conditions revealed by stress drop and b-value mapping in the northern chilean subduction zone. *Scientific Reports*, *14*(1), 12182.

Frank, W., & Shapiro, N. (2014). Automatic detection of low-frequency earthquakes (lfes) based on a beamformed network response. *Geophysical Journal International*, *197*(2), 1215–1223.

Geffers, G., Main, I., & Naylor, M. (2022). Biases in estimating b-values from small earthquake catalogues: how high are high b-values? *Geophysical Journal International*, *229*(3), 1840–1855.

Gibbons, S. J., & Ringdal, F. (2006). The detection of low magnitude seismic events using array-based waveform correlation. *Geophysical Journal International*, *165*(1), 149–166.

Glodny, J., Echtler, H., Collao, S., Ardiles, M., Burón, P., & Figueroa, O. (2008). Differential late paleozoic active margin evolution in south-central chile (37° s–40° s)–the lanalhue fault zone. *Journal of South American Earth Sciences*, *26*(4), 397–411.

Gutenberg, B., & Richter, C. F. (1944). Frequency of earthquakes in california. *Bulletin of the Seismological Society of America*, *34*(4), 185–188.

Guéguen, P., Renault, M., Bourova, E., Péquegnat, C., Cougoulat, G., Mariscal, A., ... Paul, A. (2011). Chilean aftershock network installed one week after the mw 8.8 chile earthquake: Preliminary analysis of the accelerometric data. In *Poster* (p. 1). Retrieved from `http://bdsis.obs.ujf-grenoble.fr/BDsis/`

Haberland, C., Rietbrock, A., Lange, D., Bataille, K., & Dahm, T. (2009). Structure of the seismogenic zone of the southcentral chilean margin revealed by local earthquake traveltime tomography. *Journal of Geophysical Research: Solid Earth*, *114*(B1).

Hanks, T. C., & Kanamori, H. (1979). A moment magnitude scale. *Journal of Geophysical Research: Solid Earth*, *84*(B5), 2348–2350.

Hartigan, J. A. (1975). *Clustering algorithms*. John Wiley & Sons, Inc.

Hayes, G. P., Moore, G. L., Portner, D. E., Hearne, M., Flamme, H., Furtney, M., & Smoczyk, G. M. (2018). Slab2, a comprehensive subduction zone geometry model. *Science*, *362*(6410), 58–61.

Herrmann, M., Piegari, E., & Marzocchi, W. (2022). Revealing the spatiotemporal complexity of the magnitude distribution and b-value during an earthquake sequence. *Nature Communications*, *13*(1), 5087.

Hervé, F., Godoy, E., Parada, M. A., Ramos, V., Rapela, C., Mpodozis, C., & Davidson, J. (1987). A general view on the chilean-argentine andes, with emphasis on their early history. *Circum-Pacific Orogenic Belts and Evolution of the Pacific Ocean Basin*, *18*, 97–113.

Hervé, F., Munizaga, F., Parada, M., Brook, M., Pankhurst, R., Snelling, N., & Drake, R. (1988). Granitoids of the coast range of central chile: geochronology and geologic setting. *Journal of South American Earth Sciences*, *1*(2), 185–194.

Hicks, S. P., Rietbrock, A., Ryder, I. M., Lee, C.-S., & Miller, M. (2014). Anatomy of a megathrust: The 2010 mw 8.8 maule, chile earthquake rupture zone imaged using seismic tomography. *Earth and Planetary Science Letters*, *405*, 142–155.

Hunter, J. D. (2007). Matplotlib: A 2d graphics environment. *Computing in Science & Engineering*, *9*(3), 90–95. Retrieved from `https://zenodo.org/records/15375714` ([Software]) doi: 10.5281/zenodo.15375714

Jara-Munoz, J., Melnick, D., Brill, D., & Strecker, M. R. (2015). Segmentation of the 2010 maule chile earthquake rupture from a joint analysis of uplifted marine terraces and seismic-cycle deformation patterns. *Quaternary Science Reviews*, *113*, 171–192.

Jara-Muñoz, J., Melnick, D., Li, S., Socquet, A., Cortés-Aranda, J., Brill, D., & Strecker, M. (2022). The cryptic seismic potential of the pichilemu blind fault in chile revealed by off-fault geomorphology. *Nature Communications*, *13*(1), 3371.

Lange, D., Tilmann, F., Barrientos, S. E., Contreras-Reyes, E., Methe, P., Moreno, M., ... et al. (2012). Aftershock seismicity of the 27 february 2010 mw 8.8 maule earthquake rupture zone. *Earth and Planetary Science Letters*, *317*, 413–425.

Langston, C. A., Brazier, R., Nyblade, A. A., & Owens, T. J. (1998). Local magnitude scale and seismicity rate for tanzania, east africa. *Bulletin of the Seismological Society of America*, *88*(3), 712–721.

Li, J., Hao, M., & Cui, Z. (2024). A high-resolution aftershock catalog for the 2014 m s 6.5 ludian (china) earthquake using deep learning methods. *Applied Sciences*, *14*(5), 1997.

Lieser, K., Grevemeyer, I., Lange, D., Flueh, E., Tilmann, F., & Contreras-Reyes, E. (2014). Splay fault activity revealed by aftershocks of the 2010 mw 8.8 maule earthquake, central chile. *Geology*, *42*(9), 823–826.

Lippiello, E., & Petrillo, G. (2024). b-more-incomplete and b-more-positive: Insights on a robust estimator of magnitude distribution. *Journal of Geophysical Research: Solid Earth*, *129*(2), e2023JB027849. Retrieved from `https://zenodo.org/records/8343629` ([Software]) doi: 10.5281/zenodo.8343629

Liu, C., Lay, T., Brodsky, E. E., Dascher-Cousineau, K., & Xiong, X. (2019). Coseismic rupture process of the large 2019 ridgecrest earthquakes from joint inversion of geodetic and seismological observations. *Geophysical Research Letters*, *46*(21), 11820–11829.

Lomax, A. (2001). *Nonlinloc home page.*

Lomax, A., Michelini, A., Curtis, A., & Meyers, R. (2009). Earthquake location, direct, global-search methods. *Encyclopedia of complexity and systems science*, *5*, 2449–2473.

Lomax, A., & Savvaidis, A. (2022). High-precision earthquake location using source-specific station terms and inter-event waveform similarity. *Journal of Geophysical Research: Solid Earth*, *127*(1), e2021JB023190. Retrieved from `https://zenodo.org/records/13693145` ([Software]) doi: 10.5281/zenodo.13693145

Lorito, S., Romano, F., Atzori, S., Tong, X., Avallone, A., McCloskey, J., ... Piatanesi, A.

(2011). Limited overlap between the seismic gap and coseismic slip of the great 2010 chile earthquake. *Nature Geoscience*, *4*(3), 173–177.

Madariaga, R., Métois, M., Vigny, C., & Campos, J. (2010). Central chile finally breaks. *Science*, *328*(5975), 181–182.

Mancini, S., Segou, M., Werner, M. J., Parsons, T., Beroza, G., & Chiaraluce, L. (2022). On the use of high-resolution and deep-learning seismic catalogs for short-term earthquake forecasts: Potential benefits and current limitations. *Journal of Geophysical Research: Solid Earth*, *127*(11), e2022JB025202.

Marsan, D. (2005). The role of small earthquakes in redistributing crustal elastic stress. *Geophysical Journal International*, *163*(1), 141–151.

McInnes, L., Healy, J., Astels, S., & et al. (2017). hdbscan: Hierarchical density based clustering. *J. Open Source Softw.*, *2*(11), 205.

Melnick, D., Bookhagen, B., Strecker, M. R., & Echtler, H. P. (2009). Segmentation of megathrust rupture zones from fore-arc deformation patterns over hundreds to millions of years, arauco peninsula, chile. *Journal of Geophysical Research: Solid Earth*, *114*(B1).

Met Office. (2015). Cartopy: A cartographic python library with a matplotlib interface [Computer software manual]. Exeter, UK. Retrieved from `https://zenodo.org/records/13905945` ([Software]) doi: 10.5281/zenodo.13905945

Minetto, R., Helmstetter, A., Schwartz, S., Langlais, M., Nomade, J., & Guéguen, P. (2022). Analysis of the spatiotemporal evolution of the maurienne swarm (french alps) based on earthquake clustering. *Earth and Space Science*, *9*(7), e2021EA002097.

Moreno, M., Rosenau, M., & Oncken, O. (2010). 2010 maule earthquake slip correlates with pre-seismic locking of andean subduction zone. *Nature*, *467*(7312), 198–202.

Moscoso, E. I., & Contreras-Reyes, E. (2012). Outer rise seismicity related to the maule, chile 2010 mega-thrust earthquake and hydration of the incoming oceanic lithosphere. *Andean Geology*, *39*(3), 564–572.

Mousavi, S. M., & Beroza, G. C. (2023). Machine learning in earthquake seismology. *Annual Review of Earth and Planetary Sciences*, *51*(1), 105–129.

Mpodozis, C., & Ramos, V. (1990). The andes of chile and argentina. *Circum Pacific Council Publications*, *11*, 59–90.

Neighbors, C., Liao, E., Cochran, E. S., Funning, G., Chung, A., Lawrence, J., ... Andrés Sepulveda, H. (2015). Investigation of the high-frequency attenuation parameter, kappa, from aftershocks of the 2010 m w 8.8 maule, chile earthquake. *Geophysical Journal International*, *200*(1), 200–215.

Ojeda, J., Ruiz, S., del Campo, F., & Carvajal, M. (2020). The 21 may 1960 mw 8.1 concepción earthquake: A deep megathrust foreshock that started the 1960 central-south chilean seismic sequence. *Seismological Research Letters*, *91*(3), 1617–1627.

Pedregosa, F., Varoquaux, G., Gramfort, A., et al. (2011). Scikit-learn: Machine learning in python. *Journal of Machine Learning Research*, *12*, 2825–2830. Retrieved from `https://zenodo.org/records/14627164` ([Software]) doi: 10.5281/zenodo.14627164

Peng, Z., & Zhao, P. (2009). Migration of early aftershocks following the 2004 parkfield earthquake. *Nature Geoscience*, *2*(12), 877–881.

Piquer, J., Yáñez, G., Rivera, O., & Cooke, D. (2019). Long-lived crustal damage zones associated with fault intersections in the high andes of central chile. *Andean Geology*.

Pollitz, F. F., Brooks, B., Tong, X., Bevis, M. G., Foster, J. H., Bürgmann, R., ... others (2011). Coseismic slip distribution of the february 27, 2010 mw 8.8 maule, chile earthquake. *Geophysical Research Letters*, *38*(9).

Potin, B., Ruiz, S., Aden-Antoniow, F., Madariaga, R., & Barrientos, S. (2025). A revised chilean seismic catalog from 1982 to mid-2020. *Seismological Research Letters*, *96*(1), 484–498.

Richter, C. F. (1935). An instrumental earthquake magnitude scale. *Bulletin of the Seismological Society of America*, *25*(1), 1–32.

Rietbrock, A., Ryder, I., Hayes, G., Haberland, C., Comte, D., Roecker, S., & Lyon-Caen,

H. (2012). Aftershock seismicity of the 2010 maule mw= 8.8, chile, earthquake: Correlation between co-seismic slip models and aftershock distribution? *Geophysical Research Letters*, *39*(8).

Ross, Z. E., Idini, B., Jia, Z., Stephenson, O. L., Zhong, M., Wang, X., ... et al. (2019). Hierarchical interlocked orthogonal faulting in the 2019 ridgecrest earthquake sequence. *Science*, *366*(6463), 346–351.

Ruegg, J., Rudloff, A., Vigny, C., Madariaga, R., De Chabalier, J., Campos, J., ... Dimitrov, D. (2009). Interseismic strain accumulation measured by gps in the seismic gap between constitución and concepción in chile. *Physics of the Earth and Planetary Interiors*, *175*(1-2), 78–85.

Ruiz, J. A., & Contreras-Reyes, E. (2015). Outer rise seismicity boosted by the maule 2010 mw 8.8 megathrust earthquake. *Tectonophysics*, *653*, 127–139.

Ruiz, J. A., Hayes, G. P., Carrizo, D., Kanamori, H., Socquet, A., & Comte, D. (2014). Seismological analyses of the 2010 march 11, pichilemu, chile m w 7.0 and m w 6.9 coastal intraplate earthquakes. *Geophysical Journal International*, *197*(1), 414–434.

Ruiz, S., Aden-Antoniow, F., Baez, J. C., Otarola, C., Potin, B., del Campo, F., ... Bernard, P. (2017). Nucleation phase and dynamic inversion of the mw 6.9 valparaíso 2017 earthquake in central chile. *Geophysical Research Letters*, *44*(20), 10,290-10,297. Retrieved from `https://agupubs.onlinelibrary.wiley.com/doi/abs/10.1002/2017GL075675` doi: https://doi.org/10.1002/2017GL075675

Ruiz, S., & Madariaga, R. (2018). Historical and recent large megathrust earthquakes in chile. *Tectonophysics*, *733*, 37–56.

Ruiz, S., Madariaga, R., Astroza, M., Saragoni, G. R., Lancieri, M., Vigny, C., & Campos, J. (2012). Short-period rupture process of the 2010 mw 8.8 maule earthquake in chile. *Earthquake Spectra*, *28*(1_suppl1), 1–18.

Ryder, I., Rietbrock, A., Kelson, K., Bürgmann, R., Floyd, M., Socquet, A., ... Carrizo, D. (2012). Large extensional aftershocks in the continental forearc triggered by the 2010 maule earthquake, chile. *Geophysical Journal International*, *188*(3), 879–890.

Salazar, K., & McNutt, M. (2011). Report on the 2010 chilean earthquake and tsunami response. *Reston, Virginia: US Geological Survey*.

Santibáñez, I., Cembrano, J., García-Pérez, T., Costa, C., Yáñez, G., Marquardt, C., ... González, G. (2019). Crustal faults in the chilean andes: geological constraints and seismic potential. *Andean Geology*, *46*(1), 32–65.

Satriano, C. (2021). Sourcespec–earthquake source parameters from s-wave displacement spectra. *Zenodo*. Retrieved from `https://zenodo.org/records/6954238` ([Software]) doi: 10.5281/zenodo.6954238

Scholz, C. H. (2015). On the stress dependence of the earthquake b value. *Geophysical Research Letters*, *42*(5), 1399–1402.

Schorlemmer, D., Wiemer, S., & Wyss, M. (2005). Variations in earthquake-size distribution across different stress regimes. *Nature*, *437*(7058), 539–542.

Sculley, D. (2010). Web-scale k-means clustering. In *Proceedings of the 19th international conference on world wide web* (pp. 1177–1178).

Shelly, D. R., Beroza, G. C., & Ide, S. (2007). Non-volcanic tremor and low-frequency earthquake swarms. *Nature*, *446*(7133), 305–307.

Skoumal, R. J., Brudzinski, M. R., Currie, B. S., & Levy, J. (2014). Optimizing multi-station earthquake template matching through re-examination of the youngstown, ohio, sequence. *Earth and Planetary Science Letters*, *405*, 274–280.

Steve Roecker, & Ray Russo. (2010). *Ramp response for 2010 chile earthquake.* International Federation of Digital Seismograph Networks. Retrieved from `https://doi.org/10.7914/SN/XY_2010` ([Dataset]) doi: 10.7914/SN/XY_2010

Tan, Y. J., Waldhauser, F., Ellsworth, W. L., Zhang, M., Zhu, W., Michele, M., ... Segou, M. (2021). Machine-learning-based high-resolution earthquake catalog reveals how complex fault structures were activated during the 2016–2017 central italy sequence. *The Seismic Record*, *1*(1), 11–19.

Tassara, A., Soto, H., Bedford, J., Moreno, M., & Baez, J. C. (2016). Contrasting amount

of fluids along the megathrust ruptured by the 2010 maule earthquake as revealed by a combined analysis of aftershocks and afterslip. *Tectonophysics*, *671*, 95–109.

Trugman, D. T., & Shearer, P. M. (2017). Growclust: A hierarchical clustering algorithm for relative earthquake relocation, with application to the spanish springs and sheldon, nevada, earthquake sequences. *Seismological Research Letters*, *88*(2A), 379–391.

Uieda, L., et al. (2021). Pygmt: A python interface for the generic mapping tools. *SoftwareX*, *15*, 100703. Retrieved from `https://zenodo.org/records/4592991` ([Software]) doi: 10.5281/zenodo.4592991

van der Elst, N. J. (2021). B-positive: A robust estimator of aftershock magnitude distribution in transiently incomplete catalogs. *Journal of Geophysical Research: Solid Earth*, *126*(2), e2020JB021027.

Van Rossum, G., et al. (2007). Python programming language. In *Usenix annual technical conference* (Vol. 41, pp. 1–36). Retrieved from `https://www.python.org/downloads/release/python-31111/` ([Software])

Vigny, C., Socquet, A., Peyrat, S., Ruegg, J.-C., Métois, M., Madariaga, R., ... et al. (2011). The 2010 mw 8.8 maule megathrust earthquake of central chile, monitored by gps. *Science*, *332*(6036), 1417–1421.

Vilotte, J., et al. (2011). Seismic network xs: Chile maule aftershock temporary experiment (resif-sismob). *RESIF-Réseau Sismologique et géodésique Français*.

Virtanen, P., Gommers, R., Oliphant, T. E., et al. (2020). Scipy 1.0: Fundamental algorithms for scientific computing in python. *Nature Methods*, *17*, 261–272. Retrieved from `https://zenodo.org/records/10840233` ([Software]) doi: 10.5281/zenodo.10840233

Waldhauser, F. (2001). hypodd—a program to compute double-difference hypocenter locations (hypodd version 1.0-03/2001). *US Geol. Surv. Open File Rep., 01*, *113*.

Wessel, P., Luis, J., Uieda, L., et al. (2019). The generic mapping tools version 6 [software]. *Geochemistry, Geophysics, Geosystems*, *20*(11), 5556–5564. Retrieved from `https://zenodo.org/records/3407866` ([Software]) doi: 10.5281/zenodo.3407866

White, M. C., Fang, H., Nakata, N., & Ben-Zion, Y. (2020). Pykonal: a python package for solving the eikonal equation in spherical and cartesian coordinates using the fast marching method. *Seismological Research Letters*, *91*(4), 2378–2389.

Wu, J. (2012). *Advances in k-means clustering: a data mining thinking*. Springer Science & Business Media. Retrieved from `https://scikit-learn.org/stable/modules/generated/sklearn.cluster.MiniBatchKMeans.html` ([Software])

Wu, Y.-M., Allen, R. M., & Wu, C.-F. (2005). Revised ml determination for crustal earthquakes in taiwan. *Bulletin of the Seismological Society of America*, *95*(6), 2517–2524.

Yao, D., Walter, J. I., Meng, X., Hobbs, T. E., Peng, Z., Newman, A. V., ... Protti, M. (2017). Detailed spatiotemporal evolution of microseismicity and repeating earthquakes following the 2012 mw 7.6 nicoya earthquake. *Journal of Geophysical Research: Solid Earth*, *122*(1), 524–542.

Yue, H., Lay, T., Rivera, L., An, C., Vigny, C., Tong, X., & Baez Soto, J. C. (2014). Localized fault slip to the trench in the 2010 maule, chile mw= 8.8 earthquake from joint inversion of high-rate gps, teleseismic body waves, insar, campaign gps, and tsunami observations. *Journal of Geophysical Research: Solid Earth*, *119*(10), 7786–7804.

Zhu, W., & Beroza, G. C. (2019). Phasenet: a deep-neural-network-based seismic arrival-time picking method. *Geophysical Journal International*, *216*(1), 261–273.

Figure 1.

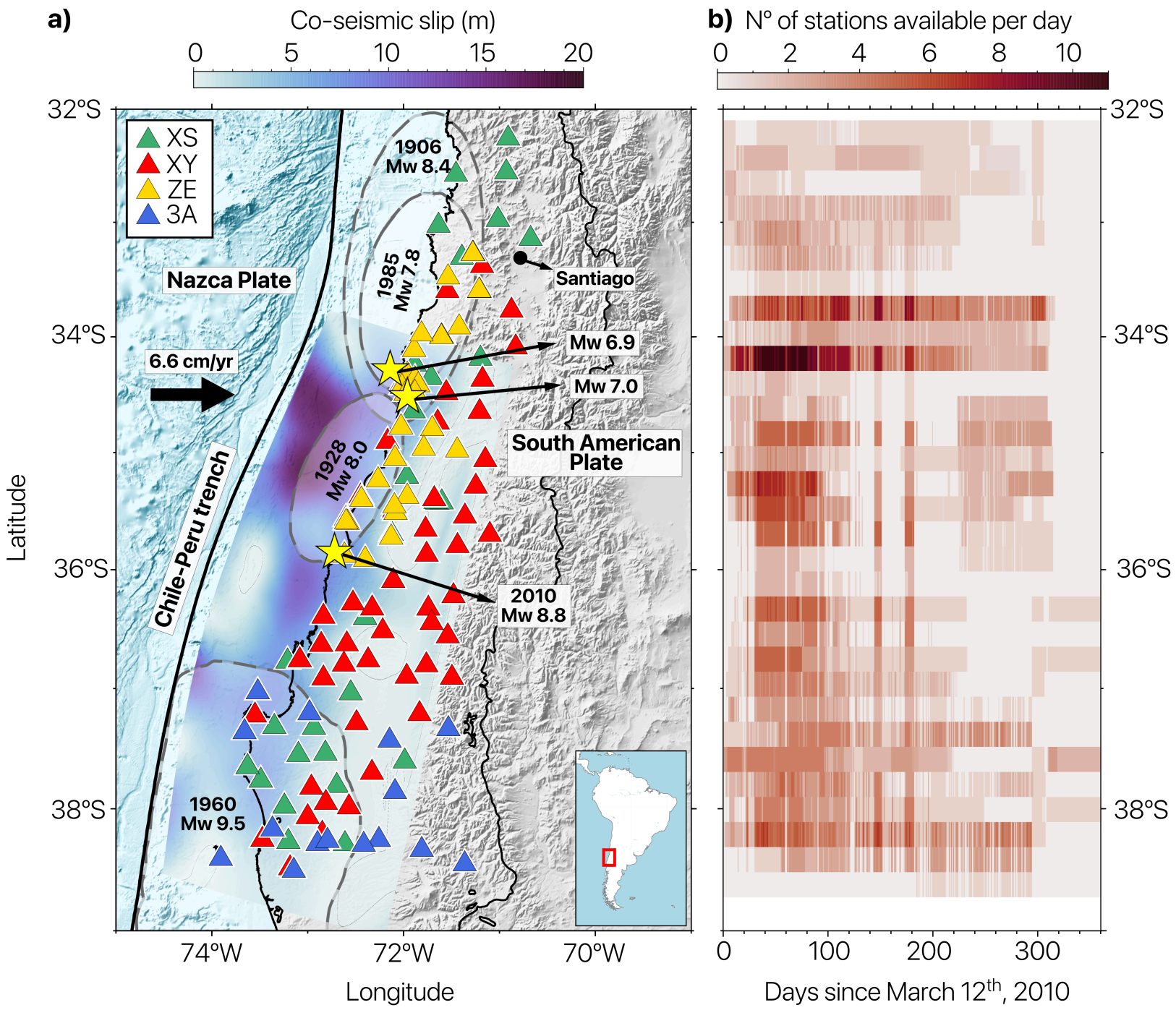
a)
Co-seismic slip (m)
0
5
10
15
20
b)
N° of stations available per day
0
2
4
6
8
10
XS
XY
ZE
3A
Nazca Plate
South American Plate
Chile-Peru trench
6.6 cm/yr
1906
Mw 8.4
1985
Mw 7.8
1928
Mw 8.0
1960
Mw 9.5
2010
Mw 8.8
Mw 6.9
Mw 7.0
Santiago
32°S
34°S
36°S
38°S
74°W
72°W
70°W
Latitude
Longitude
0
100
200
300
Days since March 12th, 2010

Figure 2.

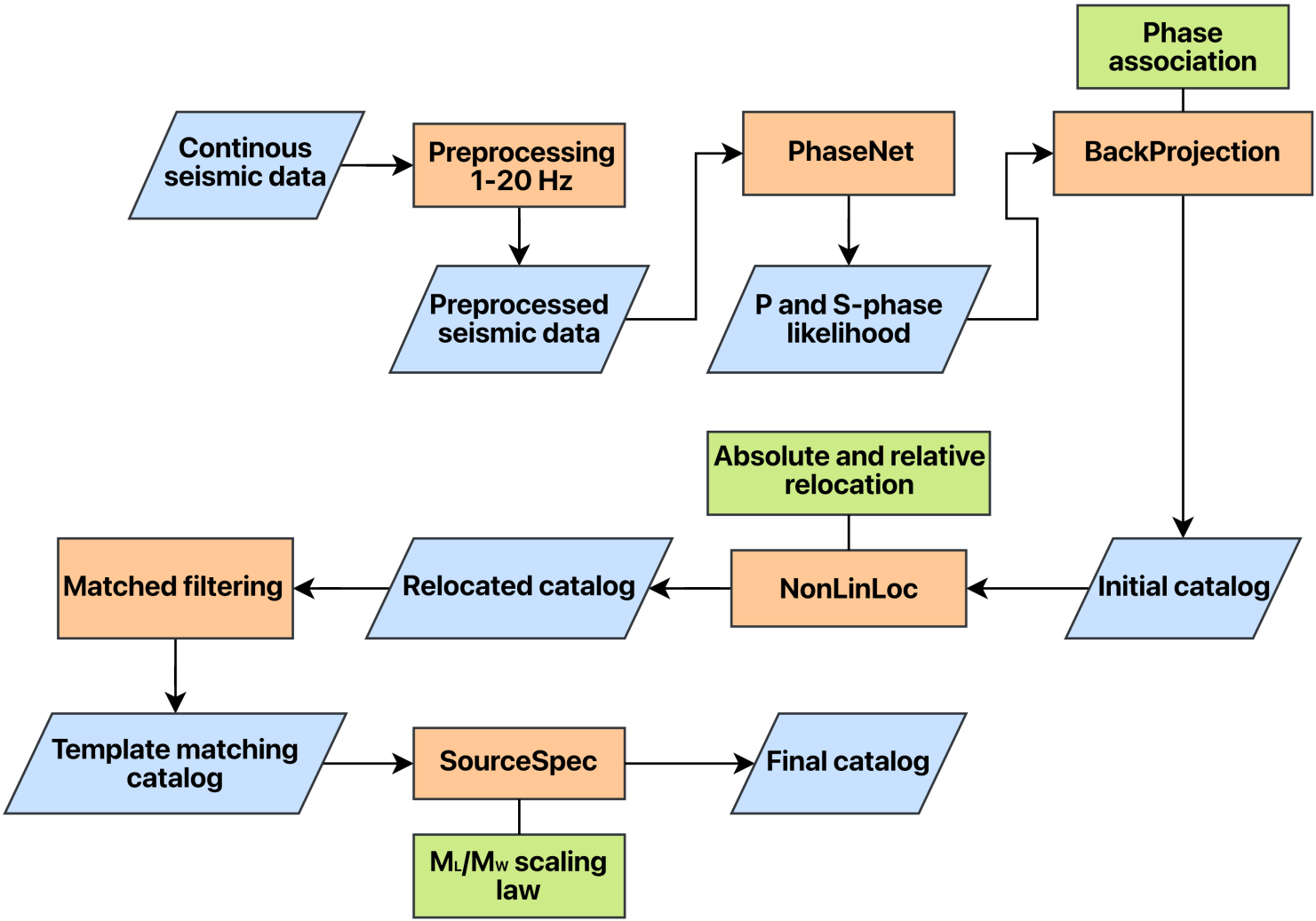
Phase association
Continous seismic data
Preprocessing 1-20 Hz
PhaseNet
BackProjection
Preprocessed seismic data
P and S-phase likelihood
Absolute and relative relocation
Matched filtering
Relocated catalog
NonLinLoc
Initial catalog
Template matching catalog
SourceSpec
Final catalog
ML/MW scaling law

Figure 3.

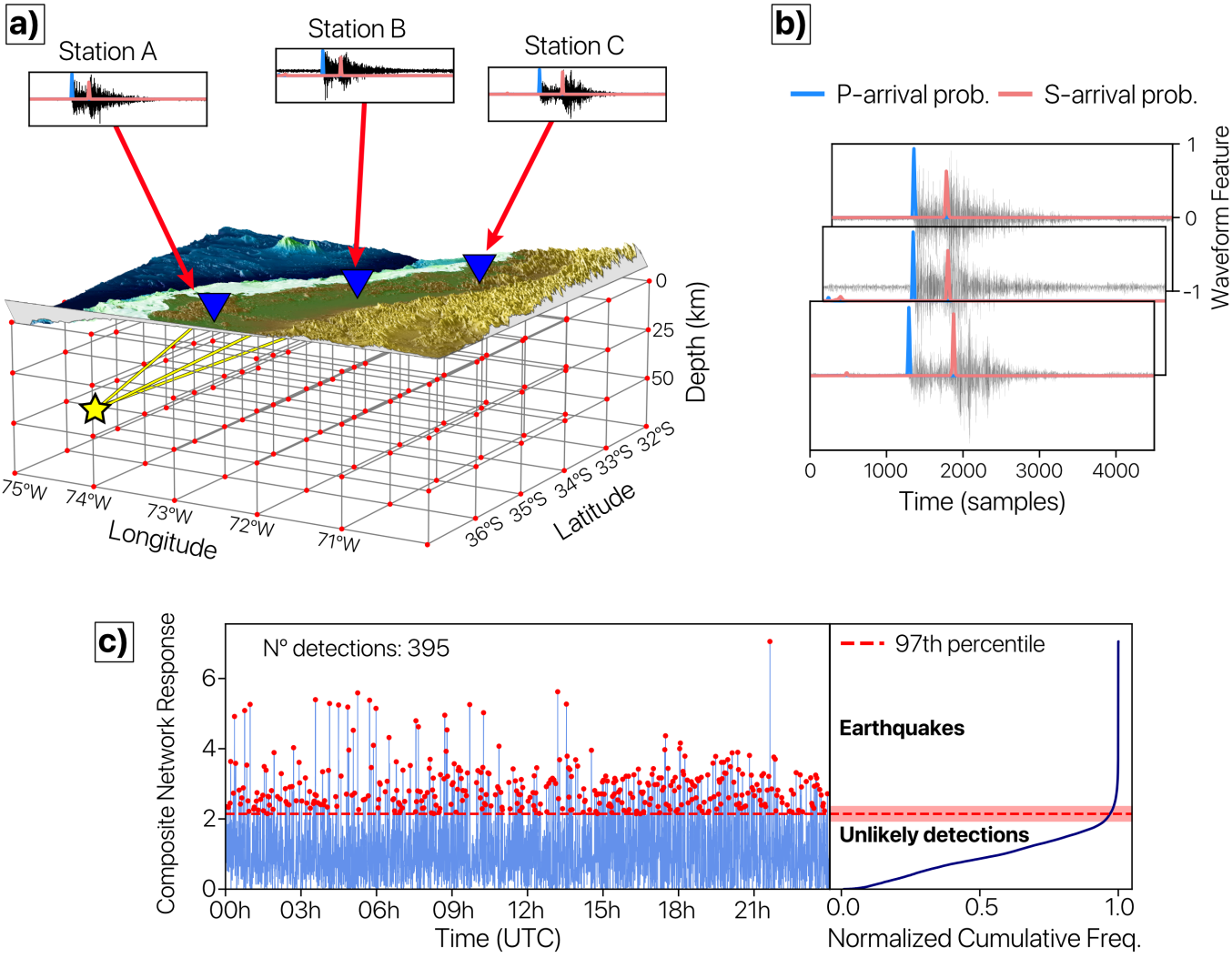
a)
Station A
Station B
Station C
Depth (km)
0
25
50
75°W
74°W
73°W
72°W
71°W
Longitude
36°S
35°S
34°S
33°S
32°S
Latitude
b)
P-arrival prob.
S-arrival prob.
Waveform Feature
1
0
-1
0
1000
2000
3000
4000
Time (samples)
c)
N° detections: 395
97th percentile
Earthquakes
Unlikely detections
Composite Network Response
0
2
4
6
00h
03h
06h
09h
12h
15h
18h
21h
Time (UTC)
0.0
0.5
1.0
Normalized Cumulative Freq.

Figure 4.

Initial location

Station residual correction

Coherence relocation

a)

b)

c)

49,230

49,230

49,230

a')

b')

c')

27,357

27,357

27,357

Latitude

Longitude

Depth (km)

0

10

20

30

40

50

>60

-32°

-34°

-36°

-38°

-75°

-73°

-71°

-69°

-34.2°

-34.4°

-34.6°

-34.8°

-72.4°

-72.2°

-72.0°

-71.8°

-71.6°

Figure 5.

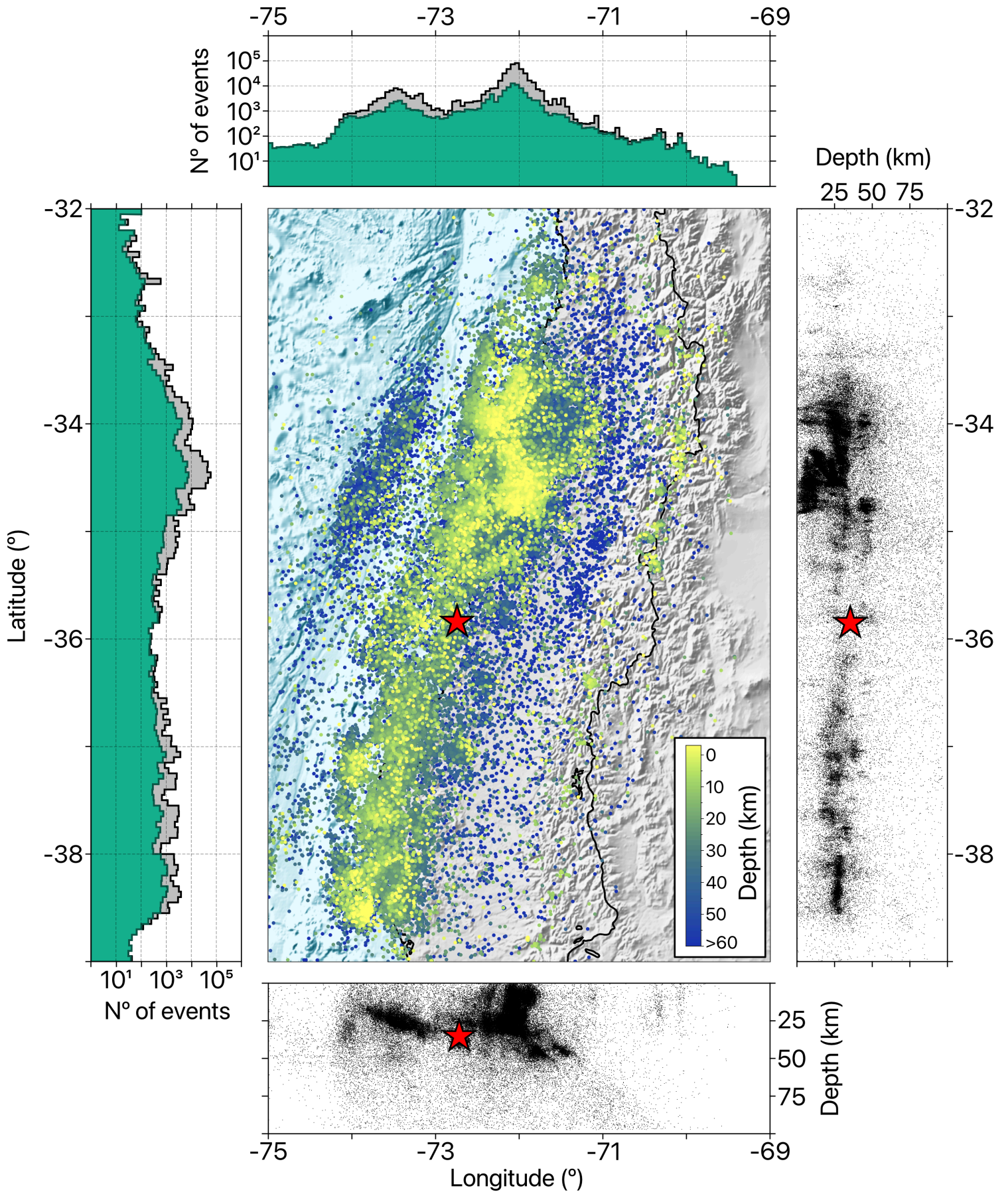
-75
-73
-71
-69
N° of events
10^5
10^4
10^3
10^2
10^1
Depth (km)
25 50 75
-32
-34
-36
-38
Latitude (°)
10^1 10^3 10^5
N° of events
0
10
20
30
40
50
>60
Depth (km)
25
50
75
Depth (km)
-75
-73
-71
-69
Longitude (°)

Figure 6.

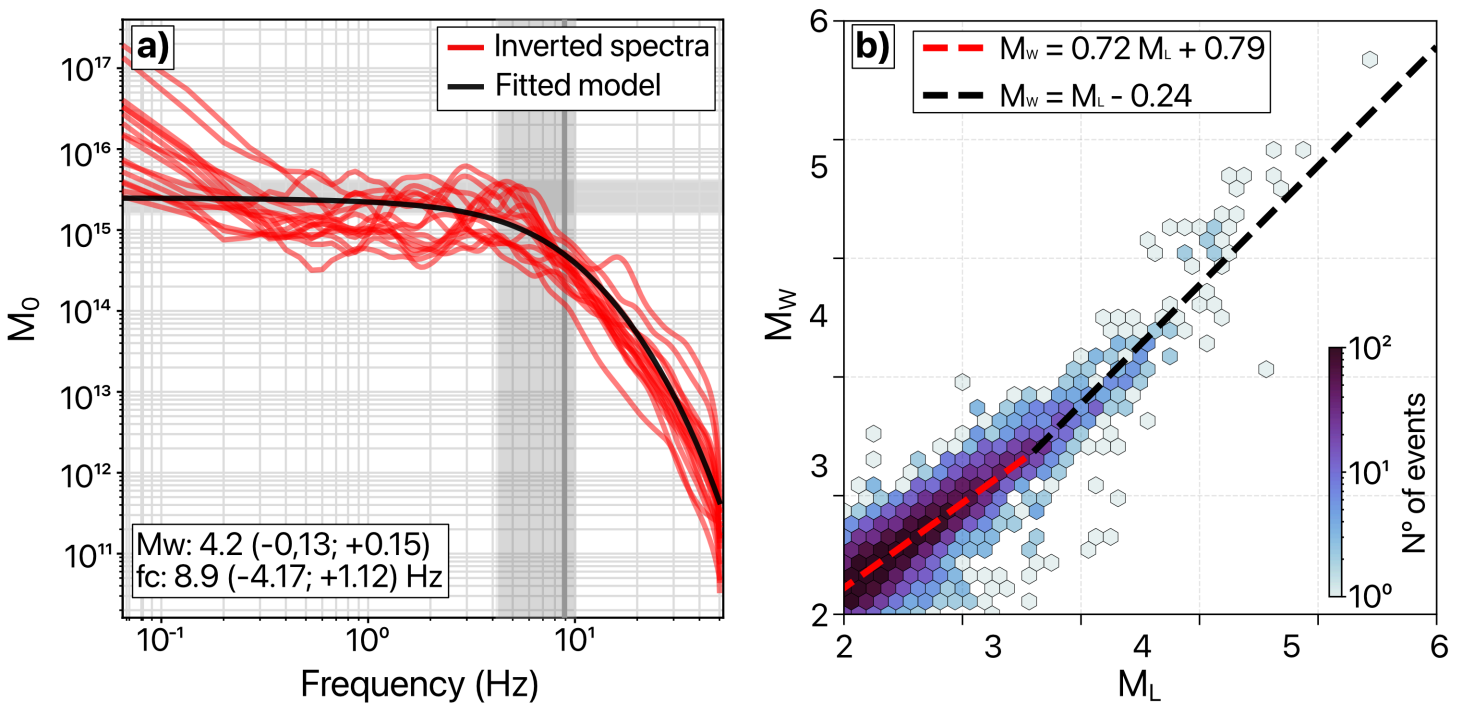
a)
Inverted spectra
Fitted model
Mw: 4.2 (-0,13; +0.15)
fc: 8.9 (-4.17; +1.12) Hz
M0
Frequency (Hz)
b)
Mw = 0.72 ML + 0.79
Mw = ML - 0.24
Mw
ML
N° of events

Figure 7.

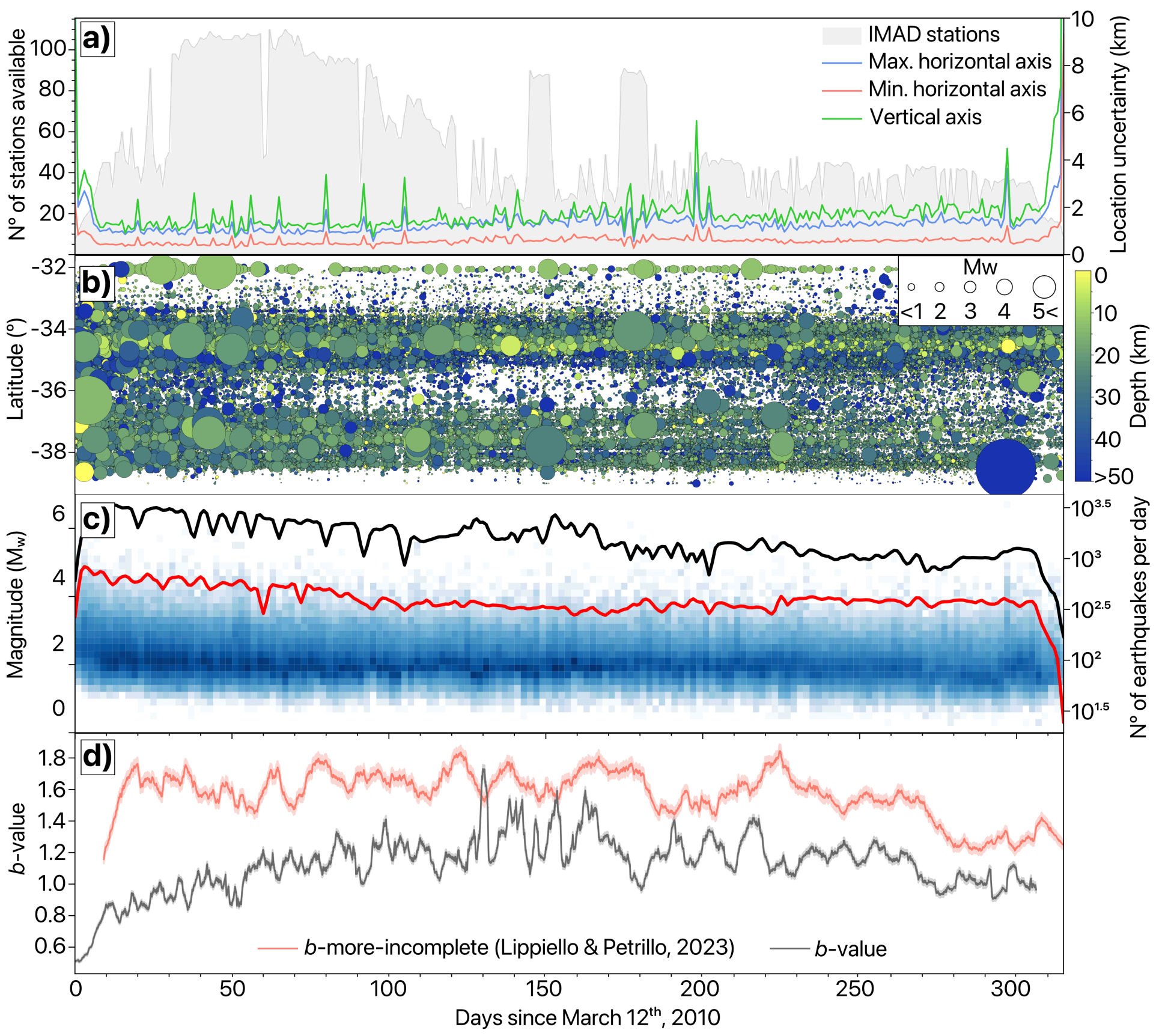
a)
IMAD stations
Max. horizontal axis
Min. horizontal axis
Vertical axis
N° of stations available
Location uncertainty (km)
b)
Mw
<1 2 3 4 5<
Latitude (°)
Depth (km)
c)
Magnitude (Mw)
N° of earthquakes per day
d)
b-value
b-more-incomplete (Lippiello & Petrillo, 2023)
b-value
Days since March 12th, 2010

Figure 8.

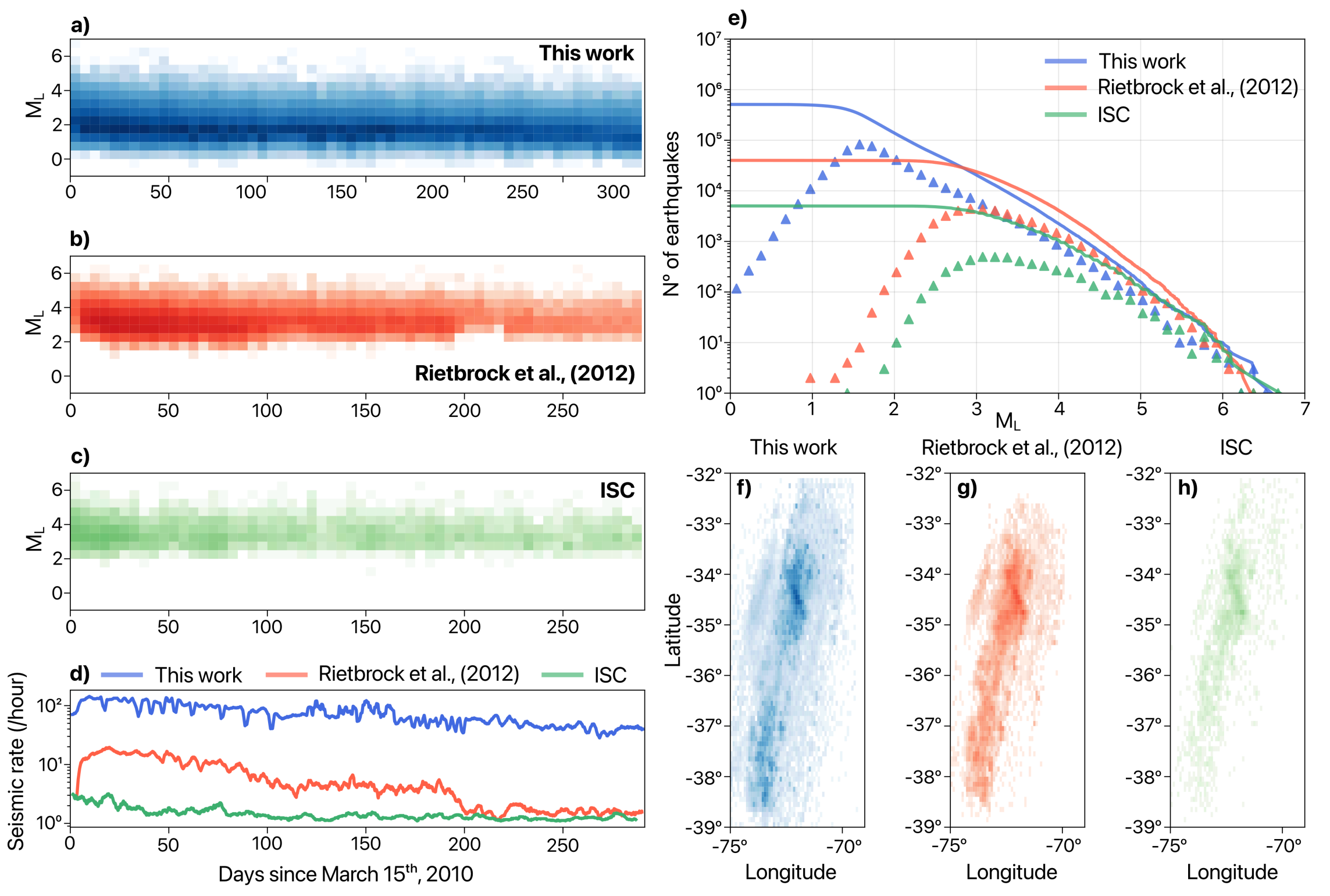
a)
This work
M_L
b)
Rietbrock et al., (2012)
c)
ISC
d)
This work
Rietbrock et al., (2012)
ISC
Seismic rate (/hour)
Days since March 15th, 2010
e)
This work
Rietbrock et al., (2012)
ISC
N° of earthquakes
M_L
f)
g)
h)
Latitude
Longitude

Figure 9.

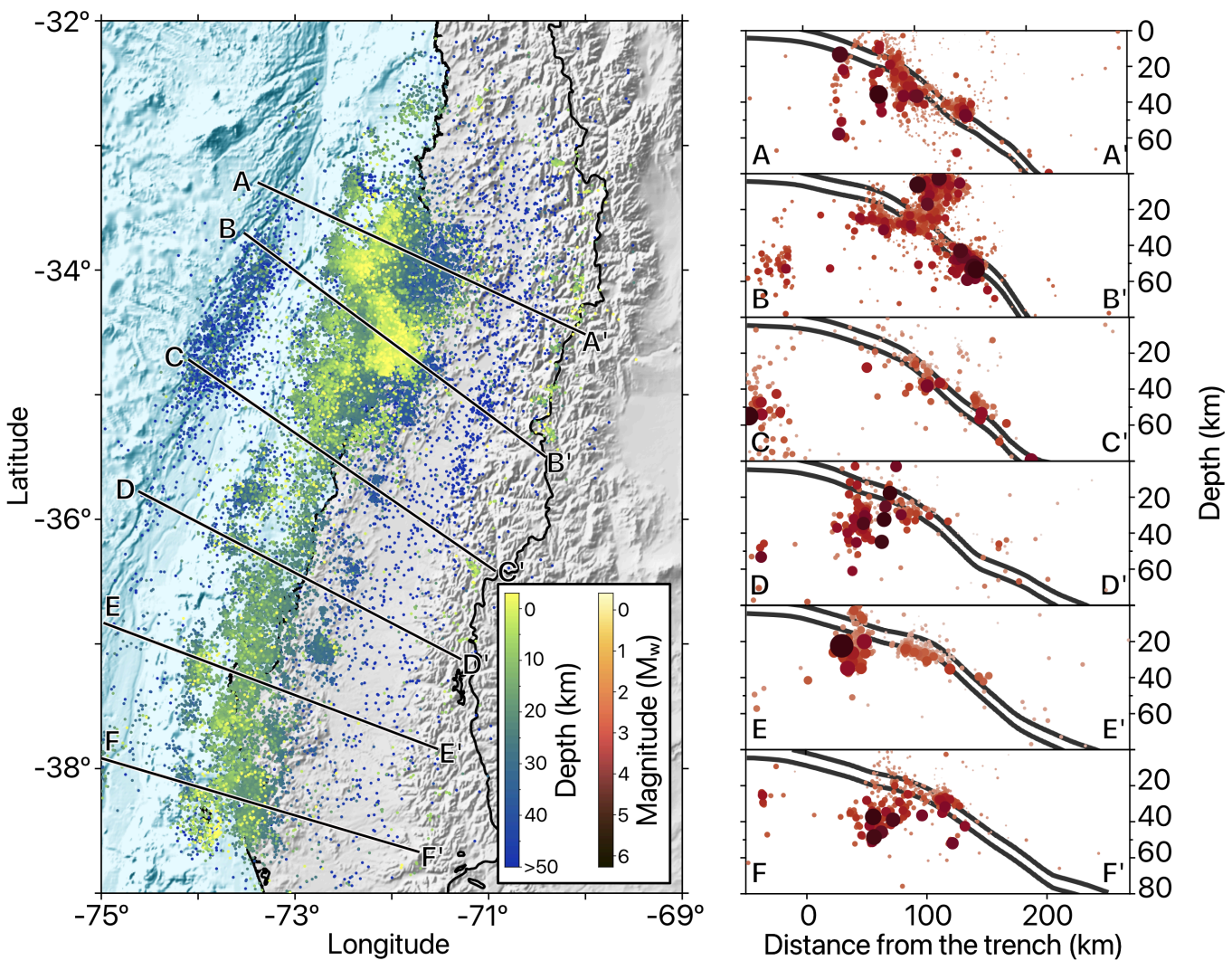
-32°
-34°
-36°
-38°
Latitude
-75°
-73°
-71°
-69°
Longitude
A
A'
B
B'
C
C'
D
D'
E
E'
F
F'
Depth (km)
0
10
20
30
40
>50
Magnitude (Mw)
0
1
2
3
4
5
6
0
20
40
60
80
Depth (km)
0
100
200
Distance from the trench (km)

Figure 10.

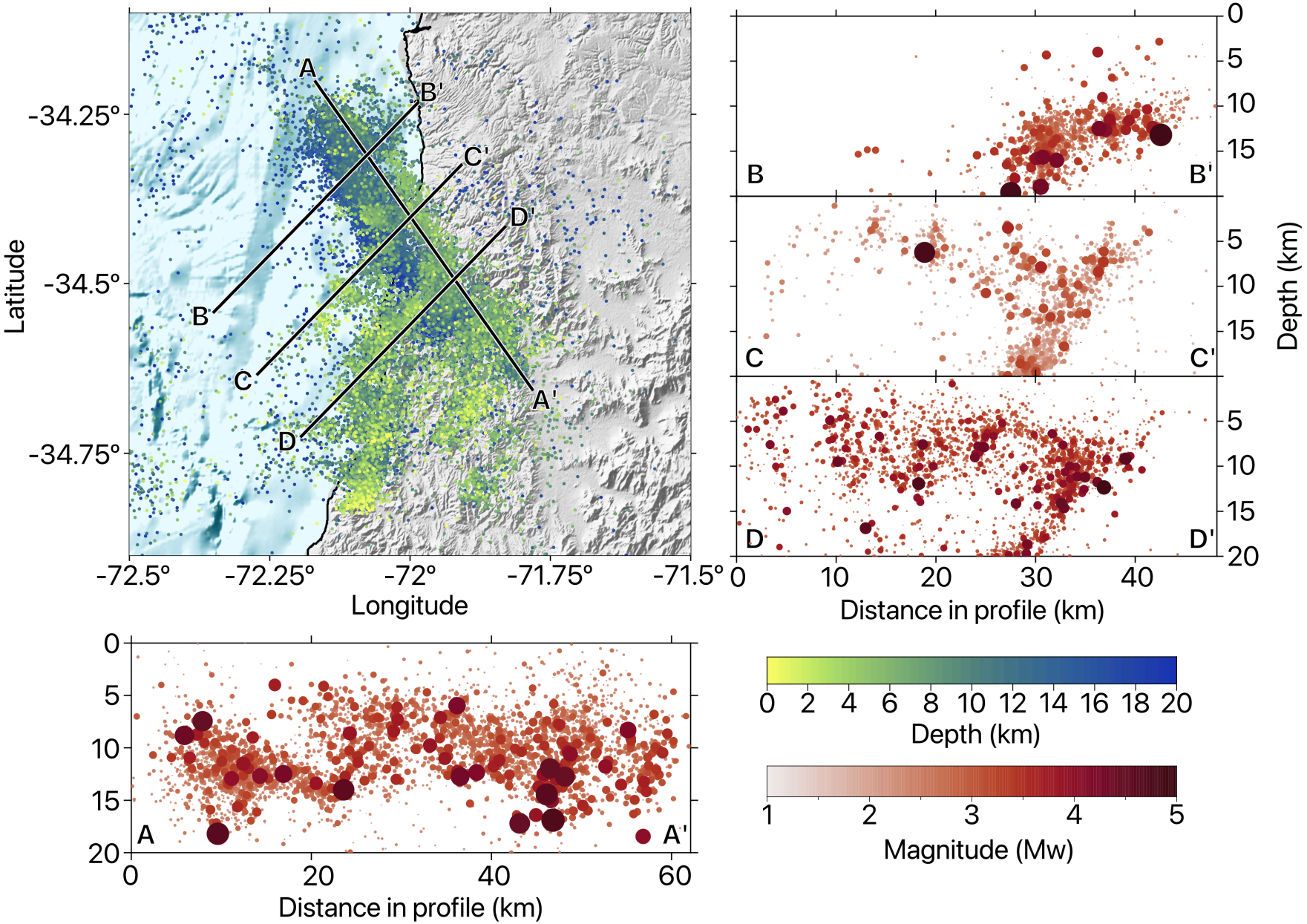
A
B'
C'
D'
B
C
A'
D
-34.25°
-34.5°
-34.75°
Latitude
-72.5°
-72.25°
-72°
-71.75°
-71.5°
Longitude
B
B'
C
C'
D
D'
0
5
10
15
20
Depth (km)
0
10
20
30
40
Distance in profile (km)
A
A'
0
20
40
60
Distance in profile (km)
0 2 4 6 8 10 12 14 16 18 20
Depth (km)
1 2 3 4 5
Magnitude (Mw)

Figure 11.

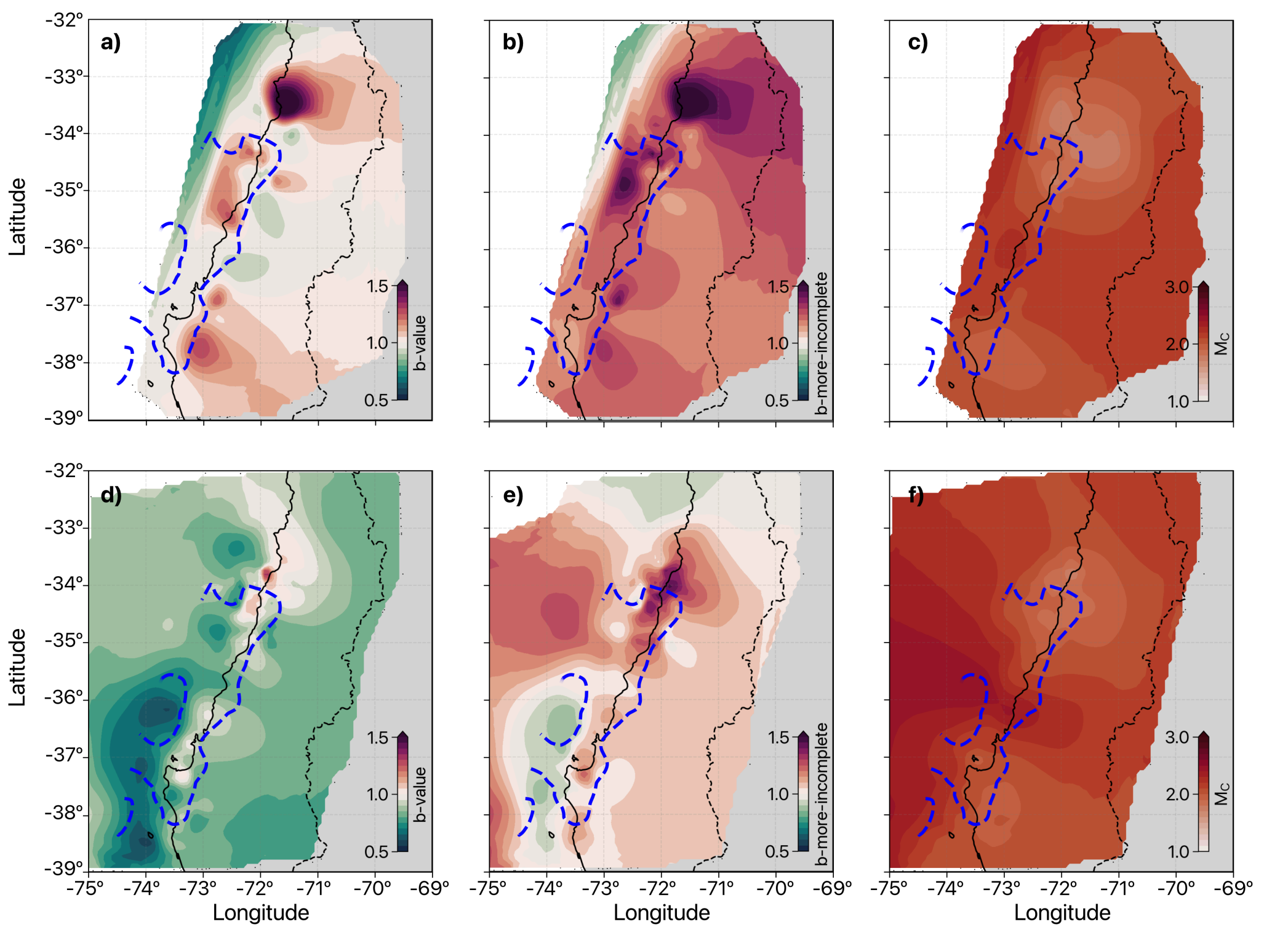
a)
b)
c)
d)
e)
f)
Latitude
Longitude
-32°
-33°
-34°
-35°
-36°
-37°
-38°
-39°
-75°
-74°
-73°
-72°
-71°
-70°
-69°
b-value
b-more-incomplete
Mc
1.5
1.0
0.5
3.0
2.0
1.0